

ADA 131788



# A REACTIVE-HEAT-PIPE FOR COMBINED HEAT GENERATION AND TRANSPORT

APPROVED FOR PUBLIC RELEASE  
DISTRIBUTION UNLIMITED

Technical Report

Sponsored by

Advanced Research Projects Agency  
ARPA Order No. 2150  
Program Code No. 2N10  
Contract No. N00609-74-C-0033

Prepared by

R-Z. You and G. M. Faath

The Pennsylvania State University  
College of Engineering  
Department of Mechanical Engineering  
University Park, Pennsylvania

December 1977

DTIC  
S  
AUG 24 1988  
C A

DTIC FILE COPY

58 08 20 050

A REACTIVE-HEAT-PIPE FOR COMBINED HEAT  
GENERATION AND TRANSPORT

Technical Report

December 1977

Sponsored by  
Advanced Research Projects Agency  
ARPA Order No. 2150  
Program Code No. 2N10  
Contract No. N00600-74-C-0033

The views and conclusions contained in this document are those of the authors and should not be interpreted as necessarily representing the official policies, either expressed or implied, of the Advanced Research Projects Agency of the U.S. Government.

Prepared by

H-Z. You  
G.M. Faeth; Telephone (814) 865-3743

Mechanical Engineering Department  
The Pennsylvania State University  
University Park, Pennsylvania 16802

DTIC  
ELECTE  
S AUG 24 1983 D  
A

REPORT DOCUMENTATION PAGE		READ INSTRUCTIONS BEFORE COMPLETING FORM
1. REPORT NUMBER	2. GOVT ACCESSION NO. AD-A131738	3. RECIPIENT'S CATALOG NUMBER
4. TITLE (and Subtitle) A Reactive-Heat-Pipe for Combined Heat Generation and Transport		5. TYPE OF REPORT & PERIOD COVERED Interim
		6. PERFORMING ORG. REPORT NUMBER
7. AUTHOR(s) H-Z. You G. M. Faeth		8. CONTRACT OR GRANT NUMBER(s) N00600-74-C-0033
9. PERFORMING ORGANIZATION NAME AND ADDRESS Department of Mechanical Engineering The Pennsylvania State University University Park, PA 16802		10. PROGRAM ELEMENT, PROJECT, TASK AREA & WORK UNIT NUMBERS 62105E, 2N10 Other DOD-ARPA, 2724-510-50
11. CONTROLLING OFFICE NAME AND ADDRESS Defense Advanced Research Projects Agency 1400 Wilson Blvd., Arlington, Va 22209		12. REPORT DATE December 1977
		13. NUMBER OF PAGES 95
14. MONITORING AGENCY NAME & ADDRESS (if different from Controlling Office) David W. Taylor Naval Ship R&D Center Annapolis, Maryland 21402		15. SECURITY CLASS. (of this report) U
		15a. DECLASSIFICATION/DOWNGRADING SCHEDULE
16. DISTRIBUTION STATEMENT (of this Report)  Approved for Public Release; distribution unlimited.		
17. DISTRIBUTION STATEMENT (of the abstract entered in Block 20, if different from Report)		
18. SUPPLEMENTARY NOTES  An M.S. Thesis in Mechanical Engineering, directed by Gerard M. Faeth		
19. KEY WORDS (Continue on reverse side if necessary and identify by block number)  Liquid Metal Combustor; Liquid Metal Reactor		
20. ABSTRACT (Continue on reverse side if necessary and identify by block number)  Over		

ABSTRACT: A reactive-heat-pipe concept is described which involves the reaction between lithium and sulfur-hexafluoride. For this concept, the lithium is evaporated from the inner surface of the wick and reacts with gaseous sulfur-hexafluoride; the energy of reaction is conducted through the wick causing lithium to evaporate from the outer surface of the wick, the vapor then transfers the energy of reaction by condensing on the heat exchanger surfaces of the load. A small combustor, generating 7.5 kW, operating at condenser temperatures of 1200 K, was designed and tested to demonstrate the operation of the concept. The system was also analyzed in order to examine the design characteristics of the wick, the vapor transport system and the condensation process on the load. The results indicate an optimum mesh size for the wick, and suggest that arterial wicks are desirable for some operating conditions. The greatest thermal resistance found in the study results from the presence of noncondensibles in the system; and several methods of control are suggested to minimize this difficulty.

Accession For

DTIC GRA&I	<input checked="" type="checkbox"/>
U.S. Army	<input type="checkbox"/>
U.S. Navy	<input type="checkbox"/>
U.S. Air Force	<input type="checkbox"/>

By \_\_\_\_\_

Distribution/Availability Codes

Dist	Avail and/or Special
A	



## TABLE OF CONTENTS

	<u>Page</u>
ABSTRACT . . . . .	iii
LIST OF TABLES . . . . .	vi
LIST OF FIGURES. . . . .	vii
NOMENCLATURE . . . . .	ix
ACKNOWLEDGMENTS. . . . .	xiii
I. INTRODUCTION. . . . .	1
1.1 General Statement of the Problem . . . . .	1
1.2 Previous Related Studies . . . . .	3
1.2.1 Submerged Injector Combustor. . . . .	3
1.2.2 Wick-Type Combustor . . . . .	7
1.3 Reactive-Heat-Pipe Concept . . . . .	12
1.4 Specific Objectives of the Study . . . . .	16
II. EXPERIMENTAL APPARATUS. . . . .	17
2.1 General Characteristics. . . . .	17
2.2 Combustor. . . . .	17
2.3 Gas Supply System. . . . .	21
2.4 Instrumentation. . . . .	24
2.5 Reactants. . . . .	26
2.6 Experimental Procedure . . . . .	26
III. EXPERIMENTAL RESULTS AND DISCUSSION . . . . .	28
3.1 Test 1 . . . . .	28
3.2 Test 2 . . . . .	30
3.3 Test 3 . . . . .	34
3.4 Test 4 . . . . .	35
3.5 Tests 5 and 6. . . . .	36
3.6 Discussion . . . . .	37
IV. THEORETICAL MODEL . . . . .	39
4.1 Wick Analysis. . . . .	40
4.2 Transport Tube Analysis. . . . .	48
4.3 Condenser Analysis . . . . .	51

## TABLE OF CONTENTS (CONTINUED)

	<u>Page</u>
4.3.1 Condensation in the Absence of Noncondensibles . . . . .	51
4.3.2 Condensation in the Presence of Noncondensibles . . . . .	54
4.4 Thermophysical Properties. . . . .	55
4.4.1 Properties of Lithium . . . . .	55
4.4.2 Properties of Argon . . . . .	59
V. RESULTS . . . . .	63
5.1 Wick . . . . .	63
5.2 Vapor Transport and Condensation . . . . .	71
5.3 Thermal Resistances in Some Typical Systems. . . . .	76
VI. SUMMARY AND CONCLUSIONS . . . . .	81
6.1 Summary. . . . .	81
6.2 Conclusions. . . . .	82
6.3 Recommendations for Further Study. . . . .	84
BIBLIOGRAPHY . . . . .	85
APPENDIX A: CALCULATION OF THE THERMAL RESISTANCE OF CONDENSATION FOR TEST 3 . . . . .	88
APPENDIX B: CALCULATION OF PROPERTIES FOR GAS MIXTURES. . . . .	91
B.1 Grashof Number . . . . .	91
B.2 Prandtl Number . . . . .	93
B.3 Schmidt Number . . . . .	93

## LIST OF TABLES

<u>Table</u>	<u>Title</u>	<u>Page</u>
1	Design Summary of the Reactive-Heat-Pipe-Combustor. . . . .	19
2	Summary of Reactive-Heat-Pipe-Combustor Tests. . . . .	29
3	Molecular Weight, Melting Point, Boiling Point and Critical Point of Argon and Lithium. . . . .	56
4	Thermophysical Properties of Lithium at Saturation Conditions . . . . .	57
5	Reliable Temperature Ranges of the Correlations for Lithium Properties . . . . .	60
6	Thermophysical Properties of Argon at Pressure of 1 Bar . . . . .	62
7	$H_{max}$ for Arterial Wicks. . . . .	72

## LIST OF FIGURES

<u>Figure</u>	<u>Caption</u>	<u>Page</u>
1	Submerged Injector Combustor . . . . .	4
2	Coaxial Injector Combustor with Recirculating Argon Shroud Flow. . . . .	6
3	Wick-Type Combustor. . . . .	8
4	Wick Combustion Process. . . . .	9
5	Combustor Pressure Versus Wick Surface Temperature . .	11
6	Reactive-Heat-Pipe Concept with External Heat Exchanger. . . . .	13
7	The Steady Reactive-Heat-Pipe Concept with Internal Heat Exchanger . . . . .	14
8	Reactive-Heat-Pipe Combustor . . . . .	18
9	Top View of Condenser Baffle Arrangement . . . . .	22
10	Schematic of Gas Supply System for Reactive-Heat- Pipe Combustor Tests . . . . .	23
11	Data from Test 2 . . . . .	32
12	Condenser Wall Temperature Distributions During Test 2 . . . . .	33
13	Sketch of the Wick Model . . . . .	41
14	Model of the Heat Transport System . . . . .	49
15	Condensation Resistances . . . . .	52
16	Wick Thermal Resistance. . . . .	64
17	Wick Thermal Resistance with Different Layers of Screen . . . . .	65
18	Wick Thermal Resistance with Different Mesh Sizes. . .	66
19	Wick Pumping Heights for Different Mesh Sizes. . . . .	68
20	Wick Pumping Heights for Different Temperatures. . . .	69

## LIST OF FIGURES (CONTINUED)

<u>Figure</u>	<u>Caption</u>	<u>Page</u>
21	Wick Pumping Heights for Different Temperatures. . . .	70
22	Effect of Flow Losses on System Thermal Performance with No Argon in the Condenser . . . . .	73
23	Flow Losses in the Vapor Transport System with Argon in the Condenser . . . . .	75
24	Temperature Distributions in a Reactive-Heat-Pipe with No Argon in the Condenser . . . . .	77
25	Temperature Distribution in a Reactive-Heat-Pipe with Various Argon Concentrations in the Condenser . .	78

## NOMENCLATURE

A	Area or Coefficient in Equation (4.24)
a	Sound Velocity
B	Coefficient in Equation (4.24)
$C_p$	Constant-Pressure Specific Heat
$\bar{C}_p$	Constant-Pressure Specific Heat Per Unit Mole
D	Diameter of Cylinder or Tube
$D_{\text{Li-Ar}}$	Binary Mass Diffusivity of Li-Ar Mixture
d	Hydraulic Diameter
d'	Wire Diameter of Screen
F	Crimping Factor of Screen
f	Fanning Friction Coefficient
G	Mass Flux
Gr	Grashof Number
g	Gravitational Acceleration
H	Wick Pumping Height
h	Heat Transfer Coefficient
$h_{fg}$	Heat of Vaporization
j	Bulk Vapor Mass Flux
K	Wick Permeability
$K_g$	Mass Transfer Coefficient
$\bar{K}$	Boltzmann's Constant
k	Thermal Conductivity
L	Liquid Surface Displacement Across the Wick, Length
M	Mach Number
$\bar{M}$	Molecular Weight

## NOMENCLATURE (CONTINUED)

$m$	Mass
$\dot{m}$	Lithium Evaporation Rate
$\dot{m}_{ox}$	Oxidizer Flow Rate
$\dot{m}'$	Liquid Lithium Flow Rate Per Unit Width of Wick
$\dot{m}''$	Mass Flux
$N$	Mesh Size of Wick Screen
$p$	Pressure
$Pr$	Prandtl Number
$\dot{Q}$	Thermal Power of the Combustor
$Q_r$	Heat of Reaction
$\dot{q}''$	Heat Flux
$R$	Universal Gas Constant, Radius
$r$	Thermal Resistance
$R_m$	Minimum Meniscus Radius
$Re$	Reynolds Number
$Sc$	Schmidt Number
$T$	Absolute Temperature
$t$	Wick Thickness
$u$	Bulk Lithium Vapor Velocity
$V$	Bulk Vapor Velocity
$W$	Mole Fraction
$X$	Parameter in Equation (4.14)
$y$	Distance from Top of the Wick
$Z$	Gas Compressibility Factor
$\Omega_D$	Collision Integral of Binary Mixture

## NOMENCLATURE (CONTINUED)

$\beta'$	Parameter in Equation (4.21)
$\gamma$	Specific Heat Ratio
$\delta$	Wire Spacing of Screen
$\epsilon$	Volume Fraction of Solid Phase in Wick or Lennard Jones Force Constant
$\epsilon'$	Wick Void Fraction
$\mu$	Viscosity
$\rho$	Density
$\sigma$	Surface Tension
$\sigma_c$	Condensation Coefficient
$\sigma_e$	Evaporation Coefficient
$\bar{\sigma}$	Lennard-Jones Force Constant

Subscripts

A	Position A in Figure 13
Ar	Argon
Ar,g'	Argon at Position g' in Figure 15
Ar,g	Argon in the Stagnant Space at Condenser
B	Body Force or Position B in Figure 13
C	Position C in Figure 13
c	Critical Point, Combustion or Condenser
ci	Inner Surface of the Condenser
co	Outer Surface of the Condenser
E	Evaporation
e	Exit of Transporting Tube
ex	Exposed Portion of the Condenser

## NOMENCLATURE (CONTINUED)

f	Liquid Property
g	Vapor Property, Stagnant Space Outside the Wick or at Condenser
g'	Position Before the Nonequilibrium Jump at Condenser
H	Position at $y = H$ in Figure 13
i	Inlet of Vapor Transporting Tube
Li	Lithium
Li-Ar	Mixture Composed of Lithium Vapor and Argon
max	Maximum
mix	Mixture
o	Space Adjacent to the Inlet of Nozzle
s	Property of Wick Material or Surface Tension
t	Vapor Transport Tube
v	Viscous
w	Wick
wi	Inner Surface of Wick or Wall
wo	Outer Surface of Wick

#### ACKNOWLEDGEMENTS

This research was supported by David W. Taylor Naval Ship Research and Development Center, Annapolis Laboratory, as Technical Agent for Defense Advanced Research Projects Agency, under contract number N00600-74-C-0033.

## CHAPTER I

### INTRODUCTION

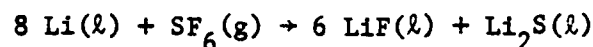
#### 1.1 General Statement of the Problem

If hydrocarbon fuels are used to fuel the power source of submersible vehicles for deep-depth operation, there are problems encountered due to volume and weight requirements and the inevitable complexity of design and construction of the exhaust system. To avoid these difficulties completely closed power systems, which use thermal energy sources, have been developed in recent years. A thermal energy source is a source of heat at an elevated temperature and can be provided by exothermic nuclear or chemical reactions. The energy released by these systems can be used to supply heat for various thermodynamic power cycles, e.g., Brayton, Stirling, Rankine, etc., which ultimately provide mechanical or electrical power.

An attractive thermal energy source for submersibles is the liquid metal combustor. The heat is generated by the chemical reaction between an alkali metal and a gaseous halogenated oxidizer. In the normal range of operating temperatures, the reaction products are in the liquid or solid state. Since the volume of the metal salts produced by reaction is nearly the same as that of the original fuel, there is no need to exhaust the products, eliminating the problem of product disposal while underwater. In addition, the liquid metal-halogen gas reactant combinations have a very high energy density providing a compact power system.

Pauluikonis [1] proposed the lithium-sulfur hexafluoride reactant combination for underwater applications. A survey of many reactant combinations by Van der Sluijs [2] also leads to the conclusion that lithium-sulfur hexafluoride was one of the best systems for underwater use. These reactants have extremely high reaction energy output, approximately the same volume of fuel and products [3], and the oxidant is nontoxic.

The reaction is completed in a combustion chamber containing the molten fuel. The oxidizer enters the chamber as a gas through an injector. The stoichiometric equation for the lithium-sulfur hexafluoride reaction is



The products of the reaction are liquids for the usual range of operating temperature [3], i.e., from 1100° K to 1200° K. The average theoretical energy release for the reaction near 1200° K is 4.75 kW-hr per kilogram of oxidizer [3]. The phase equilibrium between liquid lithium and its salts yields the formation of an immiscible liquid region and the molten bath splits into two phases. The product-rich phase settles to the bottom of the bath due to its greater density and can be accumulated and separated easily.

Thermal energy from the reaction is transferred through the walls of the combustion chamber to the working fluid of the power cycle, using a heat exchanger which is usually integral with the combustion chamber walls.

Uhlemann, Spigt, and Hermans [4], Bierman [5], and Faeth and coworkers [6-8] have investigated the metal combustors employing the lithium-sulfur hexafluoride reactant combination, demonstrating many of the operating characteristics of these systems. The overall objective of the present investigation, is to study a novel method for conducting this reaction, which provides an improved means of transporting the thermal energy of reaction to the load.

## 1.2 Previous Related Studies

1.2.1 Submerged Injector Combustor. One method of conducting the reaction involves the use of a submerged injector combustor which is illustrated schematically in Figure 1. The exit of the injector is completely submerged in the liquid fuel bath. The oxidizer passes into the combustion chamber through this injector. The reaction proceeds in a turbulent two-phase jet near the injector exit [9]. The gas is consumed and the heavy reaction products settle through the bath and are collected at the bottom of the chamber. The reaction continues, controlled by the flow rate of oxidizer, until all the fuel is consumed. At this point, the level of the product layer in the combustor is approximately the same as the initial fuel level [3].

There are several disadvantages introduced by direct oxidizer injection into the bath, in this manner, as follows:

1. The injector is subject to clogging when the oxidizer flow rate is varied [7, 8].

COMBUSTION CHARACTERISTICS

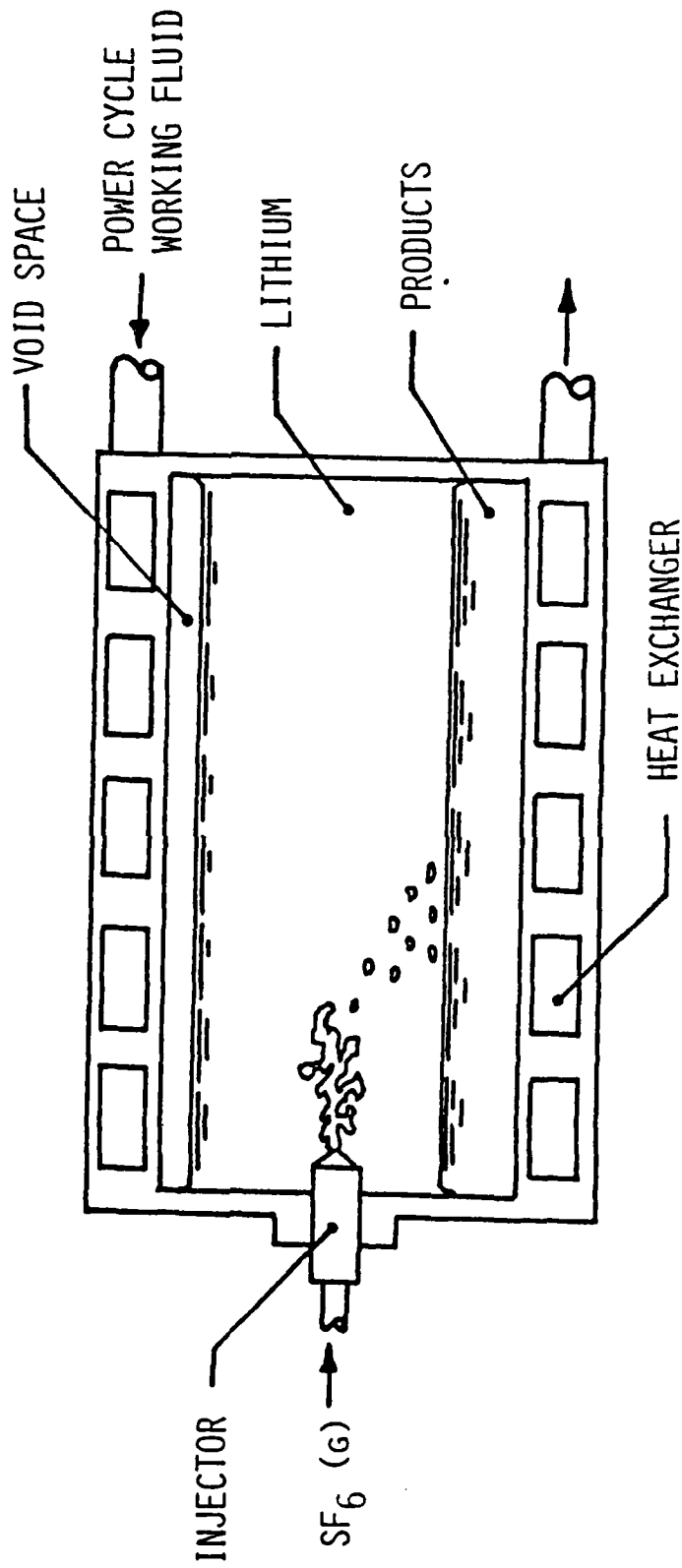


Figure 1 Submerged Injector Combustor

- ii. Due to the proximity of the molten bath, it is difficult to cool the injector, which leads to corrosion by the oxidizer.
- iii. It is difficult to restart the combustor since the injector clogs shut when the oxidizer flow is terminated.

Another approach which can resolve some of the problems of the submerged injector combustor involves the coaxial injector combustor concept, illustrated schematically in Figure 2. In this case, the injector has two passages, one for a core flow of oxidizer and a second outer shroud flow of inert gas, usually argon. The inert gas is recirculated through a vent system. The outer shroud flow prevents the direct contact between the injector body, the oxidizer, and the fuel that occurs in single passage injectors. This eliminates the possibility of unstable slugging flow which occurs when a reacting gas is injected into a liquid at a low flow rate. This type of flow instability provides the mechanism for plugging the flow passage with product material at low flow rates for a single passage injector [8]. However, problems with corrosion of the injector still exist. In addition, the coaxial injector system is more complicated than the single passage injector, tending to reduce reliability.

Another problem encountered with submerged injector systems involves the variation in bath heat transfer characteristics as the product accumulates in the combustor. Unless stirred, the product acts as a stable stratified layer, and the poor heat transfer characteristics of this region limits capabilities for transferring heat to the load.

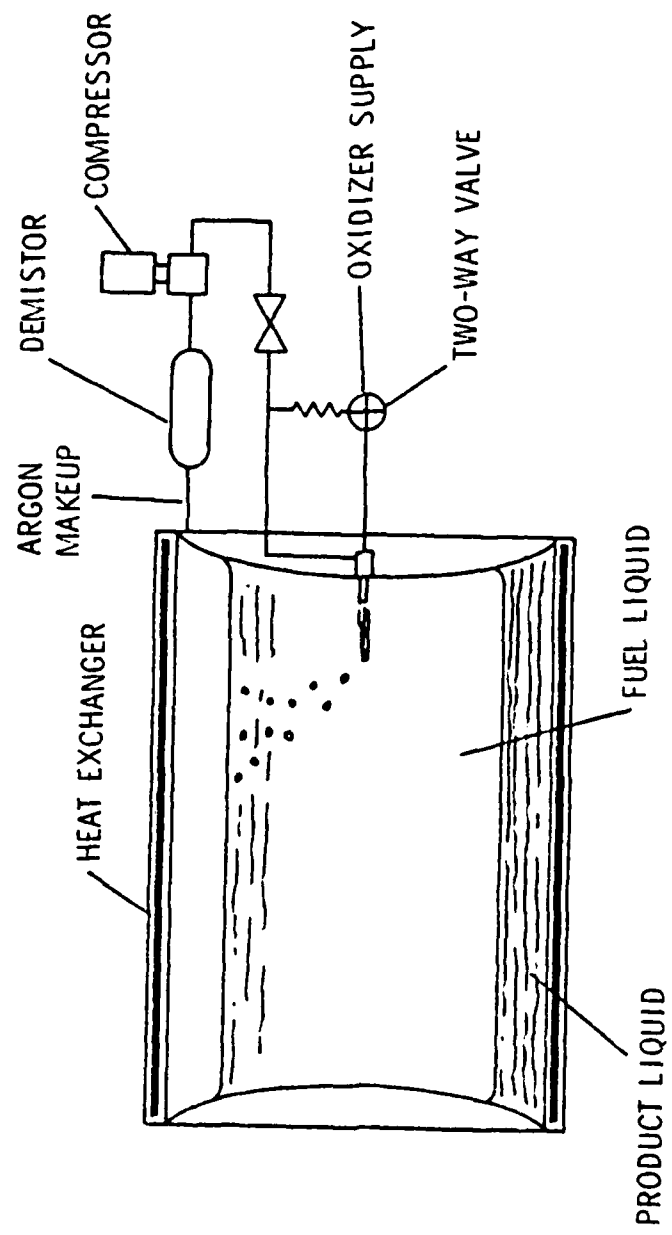


Figure 2 Coaxial Injector Combustor with Recirculating Argon Shroud Flow

1.2.2 Wick-Type Combustor. The coaxial injector meets many objectives for long-term variable load operation; however, the need to vent, filter, and recirculate the argon flow to the injector increases system complexity. In order to achieve the full capabilities of the lithium/sulfur hexafluoride reaction concept, a system which requires no argon flow must be considered. This can be done with the wick-type combustor, which is illustrated schematically in Figure 3 [10]. The arrangement is such that the lithium containing wick is mounted directly on the inside surface of the combustor, and extends below the level of the bath. The wick can control liquid motion near the injector, in order to circumvent liquid slugging in the injector passage which led to clogging of single-passage injectors at low flow rates [6]. Capillary forces draw lithium through the wick from the bath. The oxidizer passes through an injector above the liquid surface into the ullage region. The reaction proceeds as the lithium evaporates from the wick and the energy of reaction is transferred to the load through the wicking. The products condense and fall into the liquid bath at the bottom of the combustor.

Blakeslee [10] demonstrated that the combustion process occurs in the gas phase near the surface of the wick, as pictured in Figure 4. Fuel evaporates from the wick and diffuses toward the reaction zone, while the oxidizer diffuses from the ullage space to the reaction zone. The reaction proceeds as a diffusion flame, however, the products condense as they diffuse to cooler regions outside the

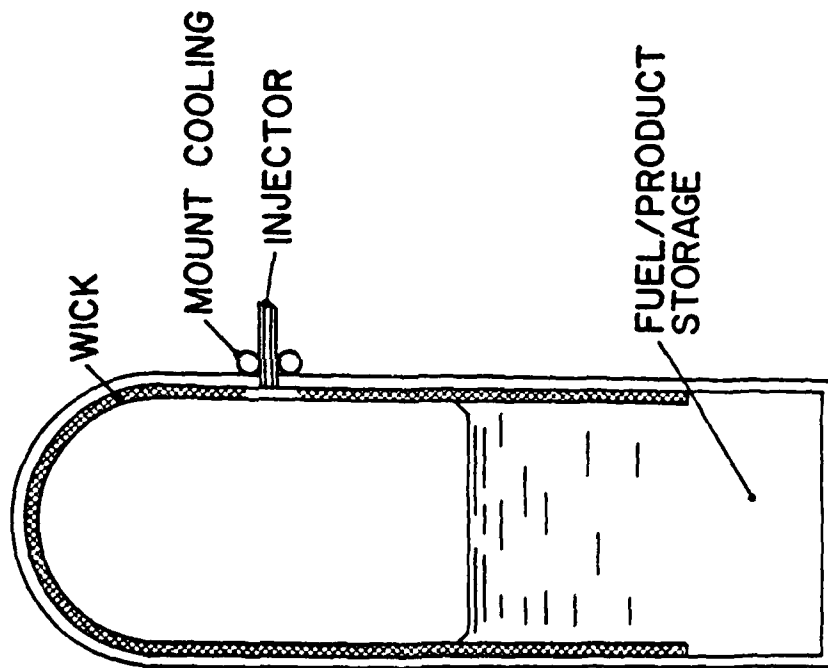


Figure 3 Wick-Type Combustor

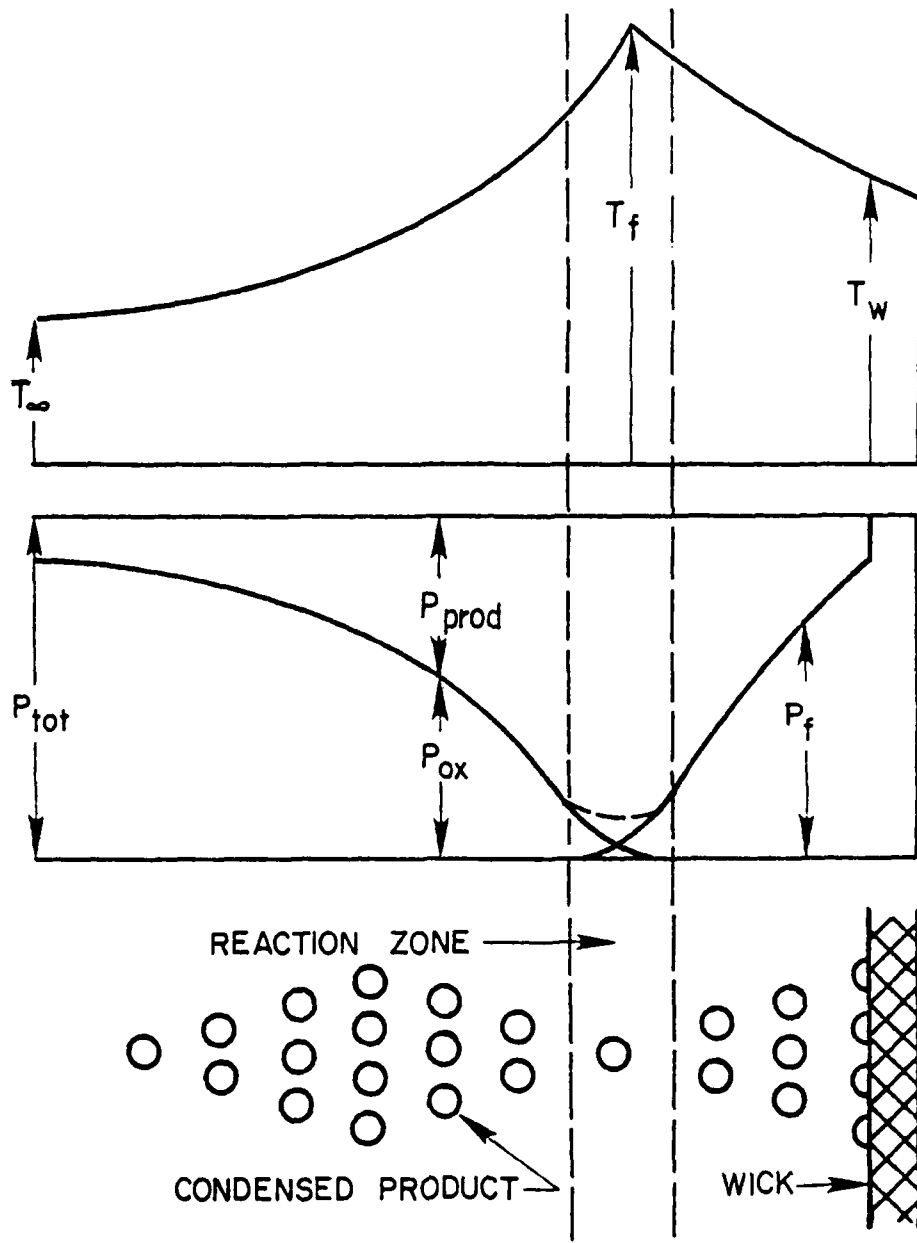


Figure 4 Wick Combustion Process

reaction zone. Some products condense on the surface of the wick, as well, in a dropwise manner [10].

For combustion rates observed during wick-type burning, gas velocities normal to the surface of the wick are small and the pressure of the process is essentially constant. This implies that the pressure within the ullage region is fixed by the vapor pressure of the fuel at the surface of the wick. Figure 5, taken from Reference [10], is an illustration of the comparison between measured pressures within the combustor and predictions based on the vapor pressure of the fuel at the surface temperature of the wick. Except at the lowest pressures where effects of noncondensibles and experimental errors are greatest, the agreement between the vapor pressure prediction and the measured pressure is reasonably good.

Heat transfer from the reaction zone to the load occurs through the wick, and is not influenced by the amount of product within the combustor. Injector reliability is also improved over submerged injector designs [4], and the complexity of a recirculating argon flow is removed. While these features are improvements over the submerged injector, several problems remain, as follows:

- i. Since the wick is fixed to the inside surface of the combustion chamber, the wick is difficult to replace.
- ii. The heat transfer characteristics of the load strongly influence wick temperatures, excessive local cooling can cause the wick to be progressively extinguished.
- iii. The configuration is relatively inflexible since the wick must cover the interior surfaces in order to prevent

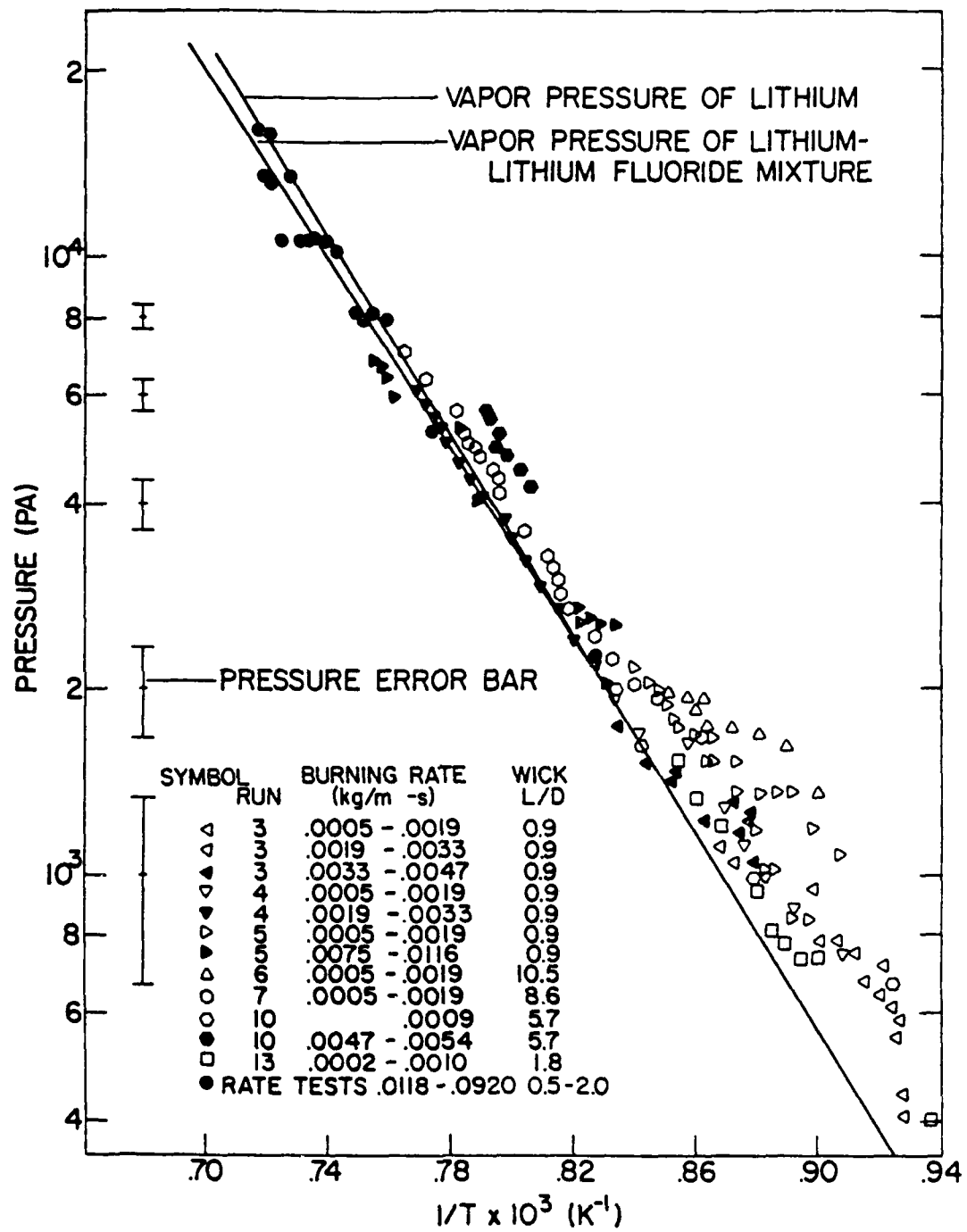


Figure 5 Combustor Pressure Versus Wick Surface Temperature

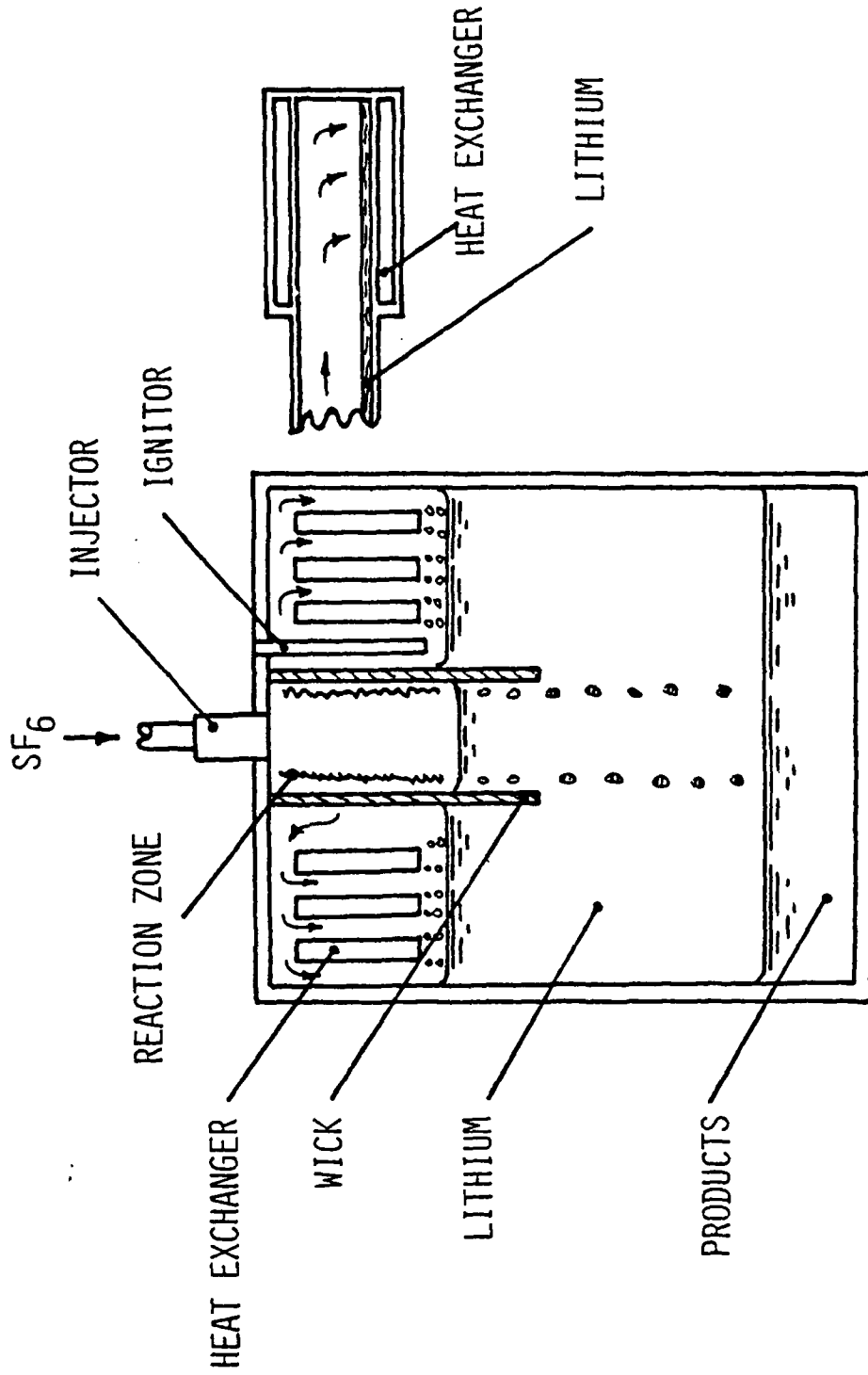
corrosion. In order to avoid wick assembly problems practical designs tends to use excessive ullage volumes, reducing system compactness.

### 1.3 Reactive-Heat-Pipe Concept

In order to overcome the problems in the wall-mounted-wick-combustor, a reactive-heat-pipe-combustor is proposed. This system combines the features of the wick-type-combustor; and a conventional heat pipe, for heat transport capabilities. The reactive-heat-pipe-combustor is illustrated in Figures 6 and 7. The heat exchanger is located outside the combustor in Figure 6 and inside the combustor in Figure 7.

The wick is free-standing in the reaction vessel, attached at its upper end at the top of the combustion chamber, and opening into the bath at the bottom. The oxidizer is injected into the space enclosed by the wick and bath. Reaction is confined within this volume, and proceeds in the same manner as the wall-mounted wick arrangement.

The energy of reaction is transported to the inside surface of the wick by convection, radiation, and condensation of the product. Then the heat is conducted through the wick and causes lithium to evaporate from the outside surface of the wick. The vapor leaving the wick flows to the heat exchanger through the gas space and then condenses to complete the transfer of reaction energy. The condensate is returned to the molten storage bath in the combustion chamber. Since the temperature of the inside surface of the wick is higher than the outside surface, there is a pressure difference across the wick.



### REACTIVE HEAT PIPE CONCEPT

Figure 6 Reactive-Heat-Pipe Concept with External Heat Exchanger

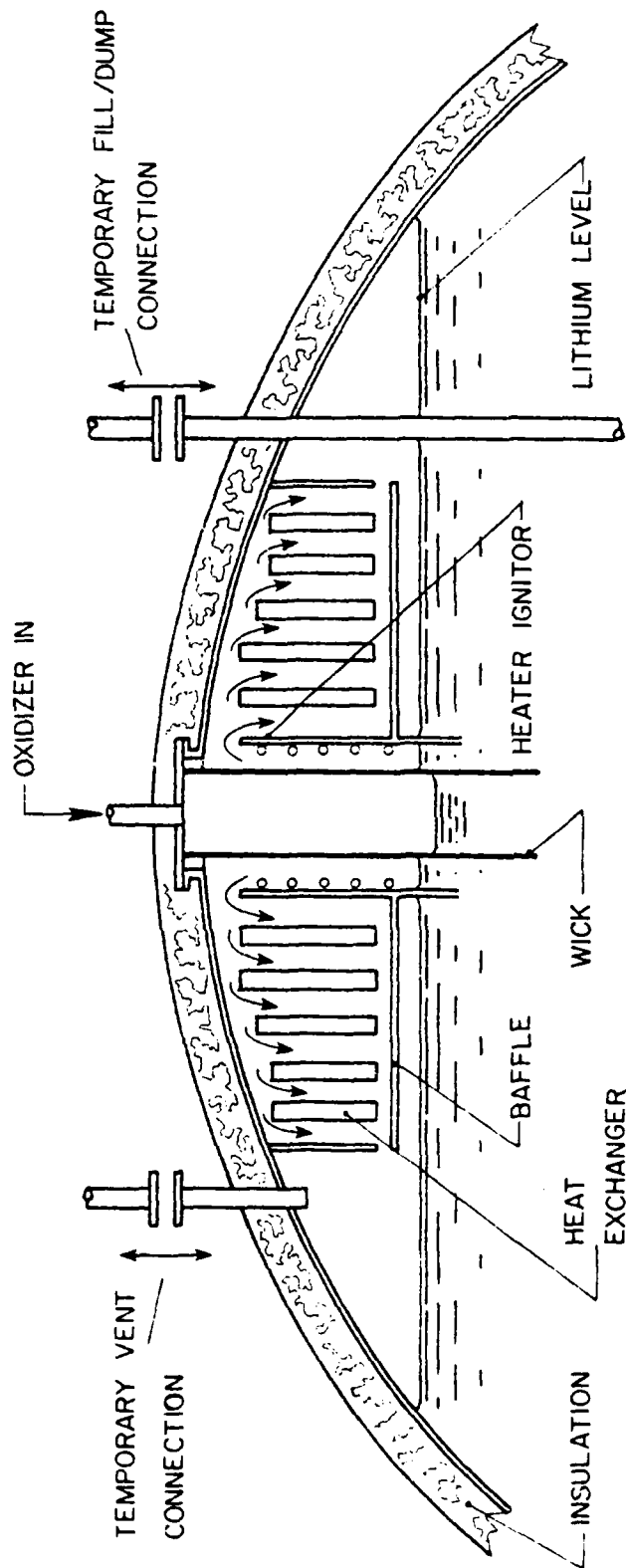


Figure 7 The Steady Reactive-Heat-Pipe Concept with Internal Heat Exchanger

This pressure difference is accommodated by a slight displacement of the liquid level under the reaction zone.

There are several advantages for this reactive-heat-pipe configuration as follows:

- i. The heat pipe for energy transfer to the load helps to maintain relatively uniform temperature distribution on both the wick and the load heat exchanger. This simplifies the design of the heat exchanger by minimizing thermal stresses.
- ii. Since the wick is free-standing in the combustion chamber, its replacement is convenient.
- iii. The wick is independent of the load, therefore, danger of local subcooling and extinguishment is eliminated.
- iv. The wick confines the reaction zone to a small volume within the combustion chamber, allowing the heat exchanger to be located in the ullage space. This conserves system volume and improves compactness.
- v. The heat pipe action allows the energy of reaction to be transported some distance from the reaction area improving the flexibility of the system layout.
- vi. The wick and the load heat exchanger have relatively small heat capacities providing rapid adjustment to load changes and a fast start. The ignitor system can also be located near the wick so that just a portion of the wick can be ignited.

#### 1.4 Specific Objectives of the Study

As discussed above, the reactive-heat-pipe-combustor has several advantages over earlier liquid metal combustors. It is capable of fast reaction to load changes; relatively fast start; flexible heat exchanger configuration; independent operation of the wick and the load heat exchanger; capability for complete shutdown and restart any number of times; and uniform temperature distributions on both the wick and the load, which simplifies the design of both these components.

While earlier work [10] has suggested the feasibility of the reactive-heat-pipe concept, this configuration has not yet been operated and its design characteristics have not been studied. Therefore, the specific objectives of the present study, are as follows:

- i. Design and test a small scale version of the reactive-heat-pipe-combustor in order to observe its practical operation.
- ii. Complete a theoretical analysis of this type of combustion system. The purpose of the analysis will be to obtain design characteristics of the wick and the heat transport system, and to investigate their performance characteristics.

The study is limited to the lithium-sulfur hexafluoride reactant combination. The principles can be applied to other reacting combinations in this family, however, these reactants appear to have the greatest advantage for practical applications.

## CHAPTER II

### EXPERIMENTAL APPARATUS

#### 2.1 General Characteristics

A combustor was designed, fabricated, and tested in order to determine the operating characteristics of the reactive-heat-pipe configuration. In order to conserve costs the combustor was relatively small, containing about .9 kg of lithium and generating a maximum thermal power of 7.5 kW. The heat exchanger for the combustor was also an inexpensive radiative-type arrangement. The load provided by the heat exchanger was controlled by moving a radiation shield over the surface of the heat exchanger.

#### 2.2 Combustor

A sketch of the reactive-heat-pipe-combustor is shown schematically in Figure 8, the major features of the design are summarized in Table 1. The combustor body is cylindrical in shape, constructed of AISI Type 316 stainless steel. The cylinder is mounted in an upright position and supported from its top flange. The combustor is filled about half-way with fuel, the lower portion acting as a fuel/product storage reservoir, the upper portion acting as the combustion area and heat exchanger.

The oxidizer enters the combustor through a nickel injector located at the center of the top flange of the combustor. The flow passage of the injector had a diameter of 10 mm. The flange area near the exit of the injector is reduced in thickness in order to minimize

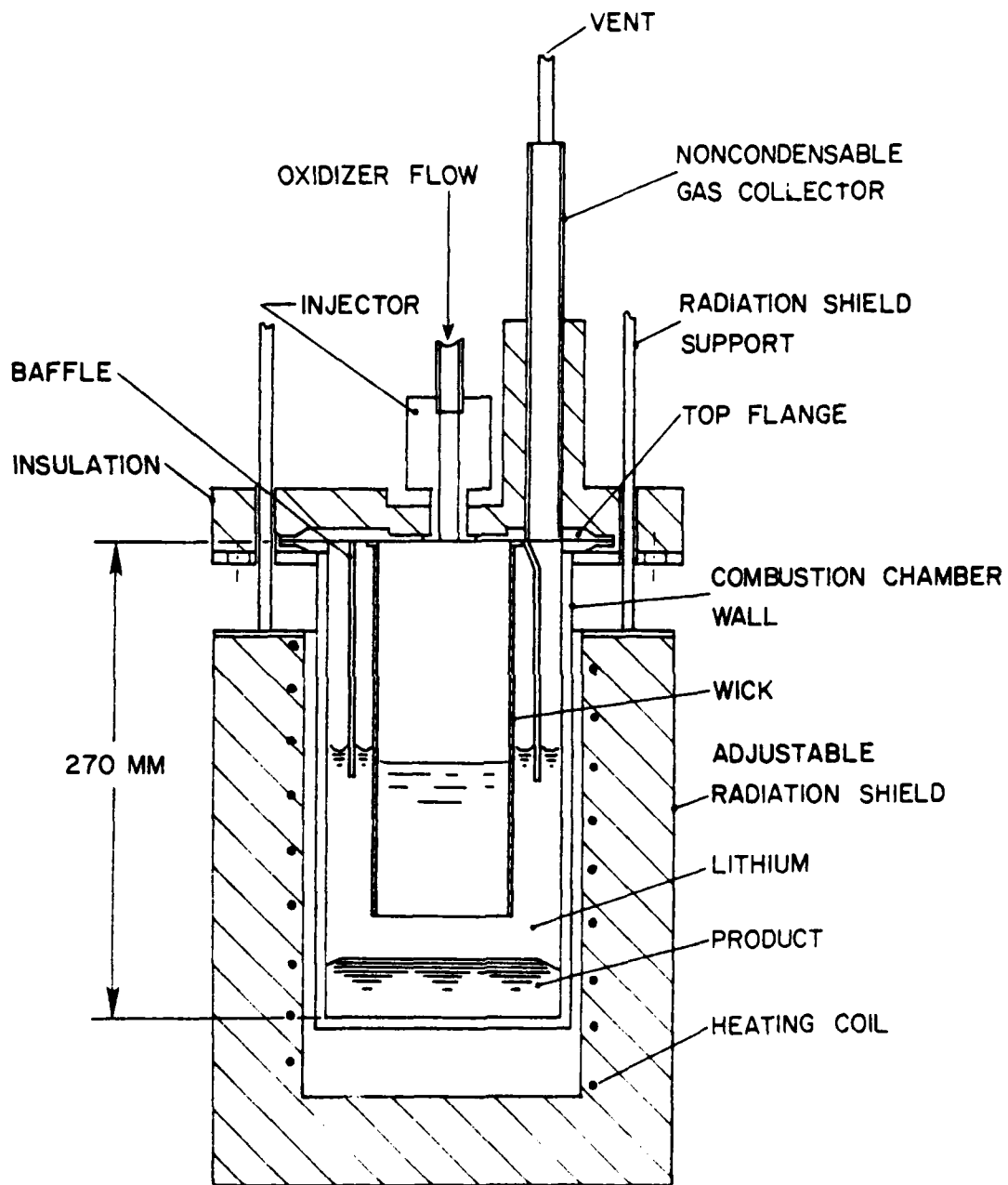


Figure 8 Reactive-Heat-Pipe Combustor

Table 1

## Design Summary of the Reactive-Heat-Pipe Combustor

Combustor	R-A
Fuel Load (kg)	0.89
Maximum Thermal Power (kW)	7.5
Combustor Diameter (mm)	128.0
Combustor Length (mm)	270.0
Wick Diameter (mm)	73.0
Active Wick Length (mm)*	125.0
Wick Aspect Ratio	1.7
Baffle Diameter (mm)	95.0
Start Heater Power (kW)	2.7

\*Distance from liquid surface to top of wick at nominal operating conditions.

the heat flow into this region and help to keep the exit area cool in order to avoid corrosion of the metal by  $SF_6$  at high temperatures. The injector also incorporated a widened cylindrical portion which provided natural convection cooling. Nickel is used in this component in order to reduce the corrosive action of the oxidizer at high temperatures.

The combustor was sealed by welding the outer edge of the top flange assembly. This edge was extended so that it could be ground away, allowing the combustor to be opened for inspection and refueling several times before replacement was necessary.

The wick is spot-welded coaxially to the top flange of the combustor and hangs down into the bath. The wick is constructed of two layers of 100-mesh type 316 stainless steel screen. The lower end of the wick extends to a position about 50 mm from the bottom of the combustor. The active area of the wick, above the liquid surface, has a length of approximately 125 mm.

The cylindrical combustor wall above the liquid level acts as the load heat exchanger. Heat is transferred from this surface primarily by radiation, with a small additional contribution from natural convection at typical operating temperatures. The rate of heat transfer from the heat exchanger is controlled by varying the vertical position of an adjustable radiation shield. The completely closed position of the shield corresponds to the no-load, idling condition.

During the course of testing it became evident that a baffle over the inside condensing surface of the heat exchanger would be

desirable in order to control the heat transfer resistance due to noncondensable gases in the system. The baffle is attached to the top of the combustor and passes around the wick in a coaxial manner. The flow of vapor from the wick to the condensing surface of the heat exchanger is illustrated in Figure 9 for both the unbaffled and baffled arrangements. The action of the baffle is to force the vapor flow into a tangential path along the surface of the heat exchanger sweeping the noncondensable gas toward a vertical collection tube located in the top flange of the combustor. The noncondensable gas can be vented from this gas collector in a manner that will be described later.

The combustor could be heated electrically in order to melt the fuel and start the combustion process. The electrical start heaters are located in the movable radiation shield. They consist of two bead heaters manufactured by the Cole-Parmer Instrument Company (Model 316-40), providing an output of 150 watts per meter of length. The total maximum power of the two heaters was 2.7 kW. The heating power was regulated by two VARIC auto transformers. The electrical heaters are insulated externally by the insulation in the radiation shield.

### 2.3 Gas Supply System

A sketch of the gas supply system is shown in Figure 10. The entire system is welded or brazed wherever possible to reduce the possibility of leakage. Those connections which could not be welded or braised were sealed with a silicon-rubber sealant. A VEECO MS-90AB

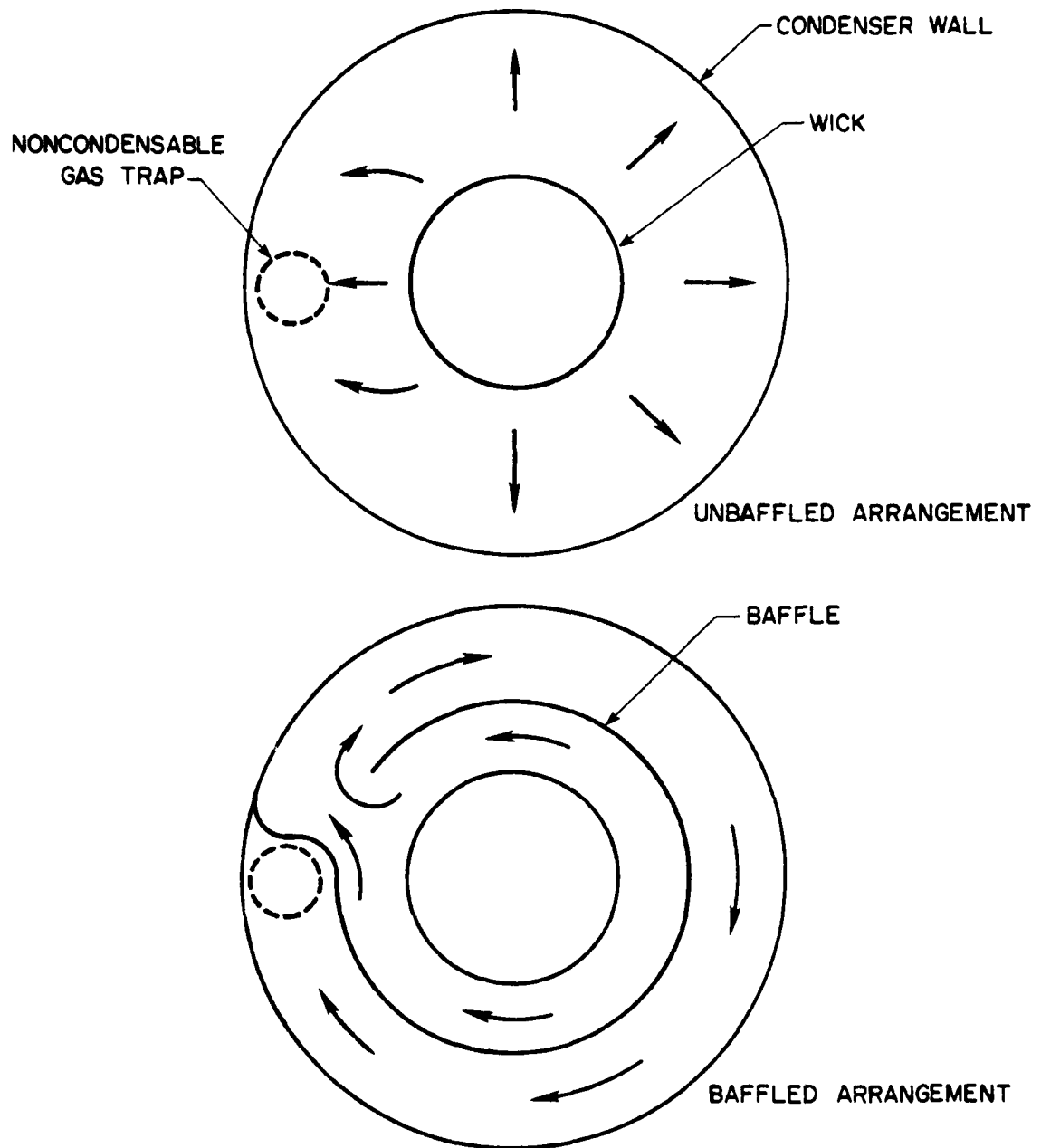


Figure 9 Top View of Condenser Baffle Arrangement

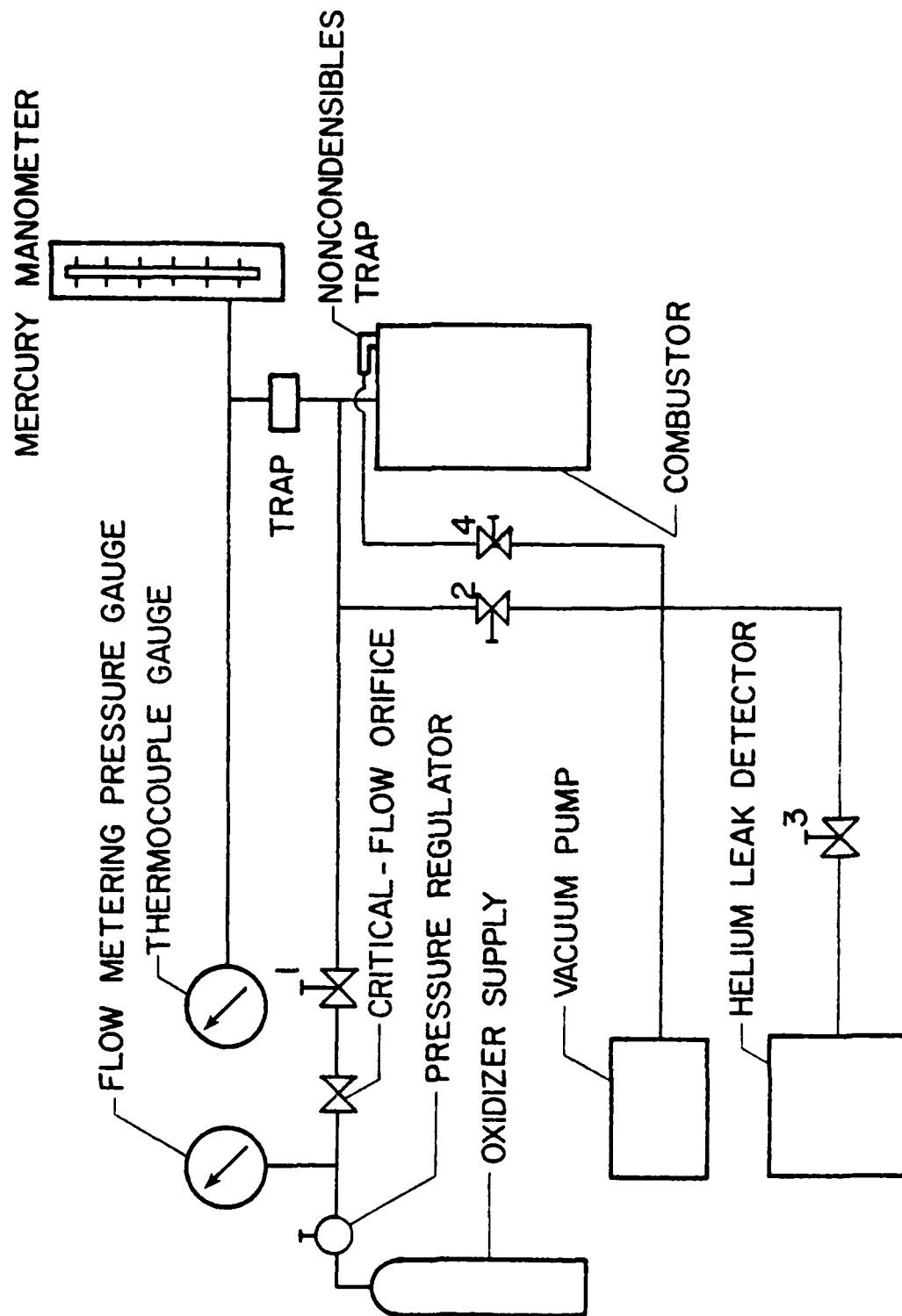


Figure 10 Schematic of Gas Supply System for Reactive-Heat-Pipe Combustor Tests

leak detector was used to helium-leak check the entire system before each test.

The oxidizer is stored as a liquid in a cylinder and drawn off from the gas phase through a pressure regulator. The oxidizer passes through a critical flow orifice which is used to meter the flow and then through the injector into the reaction region. A line near the inlet of the injector goes back to a mercury manometer and a thermocouple gage in order to record the gas pressure. The line to the pressure gages contains a trap which is used to protect the gages from contact with lithium vapors.

The combustor is connected to a vacuum pump through valve 4 on the condenser side of the wick and valve 2 on the reaction side of the wick. These connections allow noncondensibles to be removed from the system. The helium-leak detector is also connected to the vacuum side of the system through valve 3 and the load heat exchanger.

#### 2.4 Instrumentation

The oxidizer flow to the combustor was controlled by a pressure regulator and measured with a calibrated critical-flow orifice. The pressure regulator was a Matheson Model 9 two-stage regulator with 10-250 psig capability. The upstream pressure of the critical-flow orifice was measured with a Heise absolute pressure gauge (0-300 psia range with 0.5 psi divisions). The orifice was calibrated with a Precision Scientific Wet-Test Meter (0.1 cubic feet/revolution).

Combustor pressures were measured with a thermocouple vacuum gauge, Model ML-25, made by Mill Lane, Engineering Co., Inc., and an absolute mercury manometer with 1 mm subdivisions, made by Meriam

Instrumentation Co. The pressures were measured at the inlet of the injector. Since the oxidizer flows used during tests were relatively low (less than 1.5 kg/hr) the pressure drop through the injector was negligible [10]. Therefore, within the accuracy of the instrumentation, the measured pressure was equal to the combustor pressure.

The surface temperature of various components in the apparatus were measured with thermocouples. The thermocouples were constructed with chromel-alumel wire manufactured by the Thermo-Electric Company, type G/G-26-K, within American National Standards Institute limits of error of  $\pm .75$  percent in the temperature range of use. The thermocouples were spot welded directly to the combustor surfaces. There were twenty thermocouples welded to the combustor wall, 6 to the injector, 6 to the surface of the upper cover, and 4 to the noncondensibles trap. The thermocouples on the combustor wall were located in three lines, equally spaced around the periphery of the combustor, with one line directly below the inlet of the noncondensable gas trap. The vertical spacing of the thermocouples was 26 mm in the vapor region, and 78 mm in the liquid region.

Temperatures were recorded every eighteen seconds on three Leeds and Northrup Speedomax-H twelve-point recorders. The extension leads and recorders were calibrated with a Leeds and Northrup model 8686 millivolt potentiometer. The temperature-millivolt conversion values were taken from National Bureau of Standards tables.

## 2.5 Reactants

The lithium used for the tests was obtained from Lithium Corporation of America. The fuel was packed in cans and sealed under argon. The lithium is guaranteed as 99.9 percent pure with the major impurity being sodium.

The sulfur hexafluoride was obtained from Matheson Gas Products. The gas is contained in a cylinder as a liquid under its own vapor pressure (2200 KPa at 294 K). The gas was guaranteed to have minimum purity of 99.8 percent.

## 2.6 Experimental Procedure

Prior to loading the fuel, the interior of the combustion chamber and the upper cover, which is integral with injector and the noncondensibles collector, were rinsed thoroughly with methanol, then dried in a vacuum/glove box. The fuel loading steps are as follows: (1) the vacuum box was filled with argon until it reached atmospheric pressure; (2) the lithium was cleaned and weighed in the box to yield a fuel loading of around 0.9 kg; (3) the combustor was heated to 525 K in the vacuum box, melting the lithium in the combustion chamber; (4) after melting the lithium, the upper cover was aligned evenly with the combustor body and the flanges of the cover and the body were clamped together; (5) the loaded combustor was then cooled to room temperature and the venting holes, and the seam between the flanges of the cover and the body were sealed with temporary seal; (6) the combustor was then removed from the vacuum box and the top cover was seal-welded to the combustor body. During

welding a continuous argon purge was maintained into the combustor to avoid contaminating the lithium with air.

After welding, the combustor was connected to the oxidizer supply line and the vent line. Then the system was checked for leaks.

A test was begun by heating the combustor under continuous vacuum to about 850° K to degas the fuel. At this point, the vacuum pump was shut off, but heating continued. When the temperature of the bath reached 1100° K, a small amount of oxidizer was bled in the combustor. When chemical reaction began, the pressure of the combustor would suddenly drop and a sharp temperature rise of the combustor wall occurred. After ignition the oxidizer was supplied steadily and the heater was shut off.

Oxidizer flow, combustor pressure, and system temperature were recorded from the ignition point to system shut down, at intervals of 1, 2, or 5 minutes. The combustor was vented to vacuum when excessive noncondensibles accumulated in the system.

Operation was ended by gradually terminating the oxidizer flow and allowing the combustor to cool to room temperature. In order to prevent reaction with air in the event of possible leakage, the combustor ullage space was filled with argon when the combustor was stored.

## CHAPTER III

### EXPERIMENTAL RESULTS AND DISCUSSION

Six reactive-heat-pipe combustor tests were conducted, Table 2 summarizes the overall characteristics of these tests. The main objectives of the tests were to demonstrate the feasibility of the concept, to check the operation of the combustor, and to improve the design on the basis of observed operating characteristics. In the following the results for each test are discussed in detail.

#### 3.1 Test 1

This test was conducted to gain familiarity with the test apparatus and the combustor. No attempt was made to achieve good fuel utilization, therefore, the fuel utilization in this test is rather low. The combustor was operated for a period of 4.3 hours, and then shut down as planned. No difficulties were encountered with respect to injector operation or clogging. The major problem during the test was insufficient condenser action which prevented operation at high heat flux. Therefore, the power density on the wick for this test is rather low. The poor condenser action was attributed to the presence of small quantities of noncondensable gas between the wick and the condenser surface. The quantities were small, since combustor pressure levels were normal for the temperature levels of the combustor. Even small quantities, however, can inhibit condenser action, since the vapor sweeps the noncondensable gas against the

Table 2

## Summary of Reactive-Heat-Pipe Combustor Tests

Test	Run Length (hours)	Wick Power Density (W/cm <sup>2</sup> )	Maximum Wall Temperature (° K)	Fuel Utilization (%)	Type
1	4.3	1.7 - 4.5	1240	34	--
2	4.2	2.6 - 26.0	1180	96	Gas Trap
3	3.1	Idle - 26.0	1120	97	Gas Trap
4	3.2	Idle - 26.0	1150	100	Gas Trap & Baffle
5	3.0	Idle - 26.0	1220	---	Gas Trap & Baffle
6	1.3	Idle - 8.7	1200	95*	Restart, Gas Trap & Baffle

\*Combined utilization for a restart, including fuel consumed during Test 5.

condenser surface providing a diffusional barrier to the condensation process.

The combustor was disassembled after the test in order to examine the interior components. No corrosion was evident in the injector area. The wick was wetted (to the top) with lithium verifying the design of the wick assembly. The wick was also in good condition, with no evidence of corrosion.

These results verify the general operation of the reactive heat pipe combustor, and the design procedures used for wick fabrication. The results also indicated, however, that corrective action was required in order to reduce the heat transfer resistance of the condenser due to the presence of noncondensibles.

### 3.2 Test 2

In order to control the quantities of noncondensable gas within the condenser area, a vertical condenser tube was installed for this test, as shown in Figure 8. A vent line at the upper end of the condenser tube allowed noncondensable gases to be removed from the system.

When noncondensable gas was present in the condenser region, it impeded heat transfer and cool dark spots appeared on the combustor wall, particularly near the noncondensable gas trap. After the gas was vented from the trap, the combustor wall became uniformly bright red. It was only necessary to remove gas at the start of the test; no additional accumulation was observed as the test proceeded. The amount of noncondensable gas in the trap could be determined by

measuring the length of the cool dark area at the top of the condenser tube, where condensing action was inhibited.

Figure 11 is a plot of the oxidizer flow rate, the combustor pressure, and the average temperature of the condenser wall during the test. The oxidizer flow rate was adjusted to maintain the condenser wall temperature near 1150 K, and the load was varied by shifting the position of the heat shield. Since the combustor temperature was nearly constant, the combustor pressure did not vary greatly as the load was changed.

During the high load period, beginning at 180 minutes, the condenser wall temperature dropped somewhat, and the combustor pressure increased, indicating an increase in the temperature of the wick. Due to the greater heat flux through the wick at this condition, some increase in combustor pressure is expected at high loads. The pressure change observed in Figure 11, however, is greater than is predicted from Figure 5 for these operating conditions. This observation suggests that small quantities of noncondensibles were still present on the main condensing surface of the combustor, even though the vertical condenser tube removed most of the gas.

Figure 12 illustrates the temperature distribution along the combustor wall at various load conditions (note that distance is plotted from the top of the combustor, so that the condenser area is in the lower portion of each figure but above the liquid level. At full load conditions, the condenser wall temperature is nearly constant, which illustrates the desirable characteristics of the

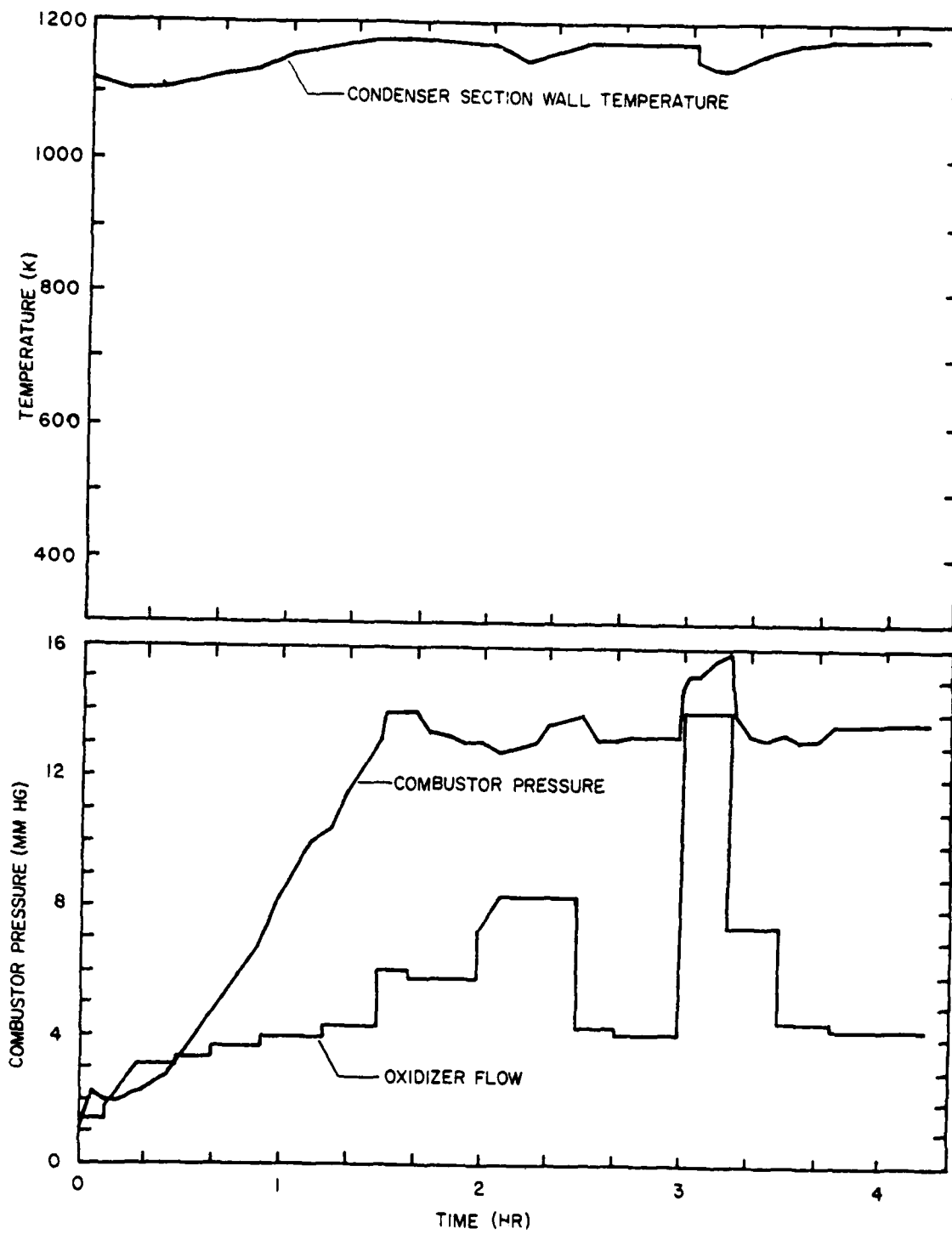


Figure 11 Data from Test 2

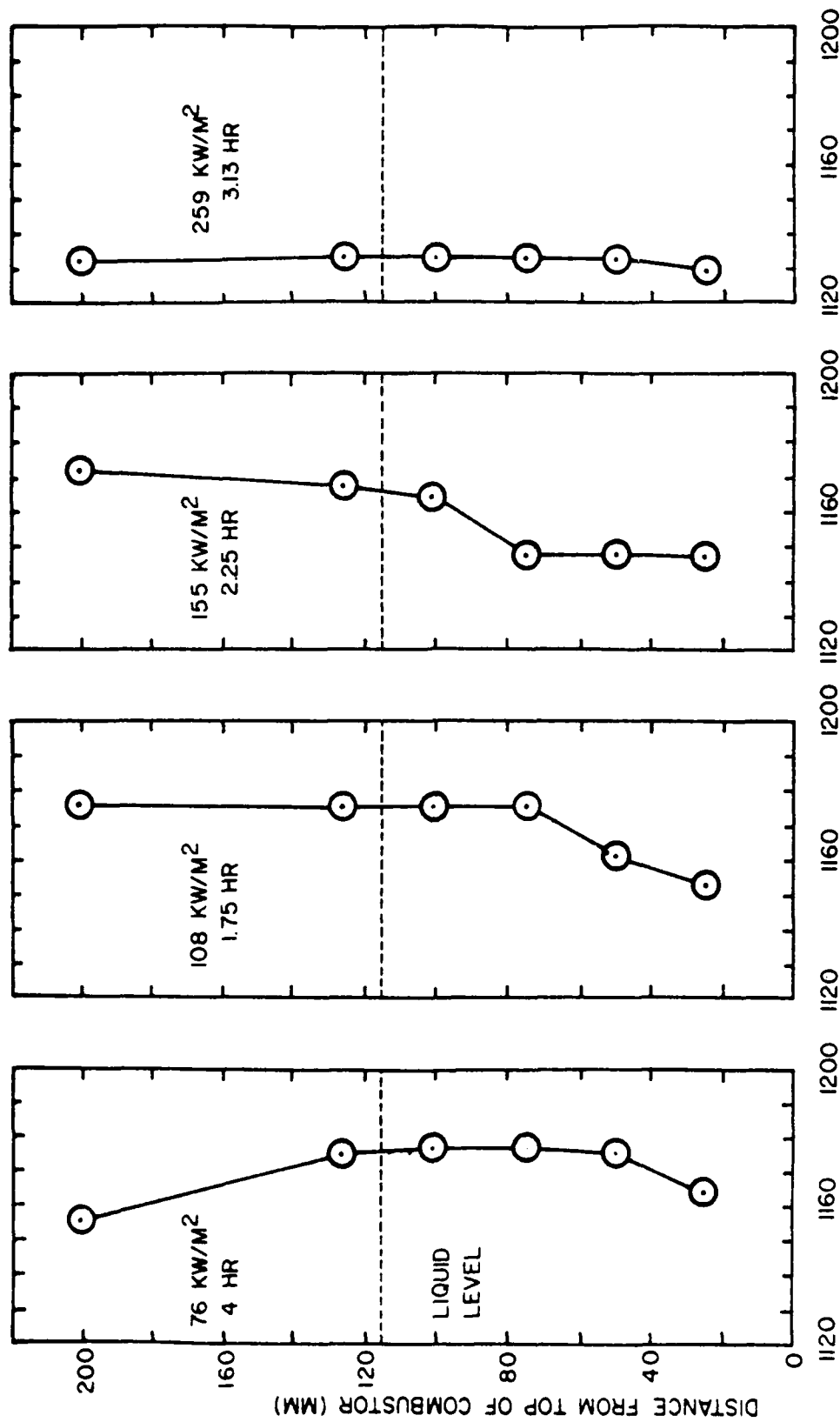


Figure 12 Condenser Wall Temperature Distributions During Test 2

WALL TEMPERATURE (K)

DISTANCE FROM TOP OF COMBUSTOR (MM)

LIQUID LEVEL

heat-pipe principle utilized in this combustor. Part load is achieved by removing the radiation shield. Under these conditions the upper portion of the condenser is operating at full load, while the lower portion is essentially at an idle condition. This leads to some loss of temperature uniformity, although the variation does not exceed 20 K. Even this variation is somewhat larger than would be predicted, due to the presence of small amounts of noncondensable gas, as discussed earlier.

The combustor was operated until pressures began to rise, indicating that the fuel was nearly consumed. At this point the operation of the combustor was terminated. The overall fuel utilization of this test was 96%, which is quite satisfactory.

After disassembling the combustor, inspection of the interior components indicated that the injector and the wick were in excellent condition.

### 3.3 Test 3

The combustor arrangement for this test was the same as Test 2. This test was somewhat shorter than the previous test, since there were two one-half hour periods, at full load, as opposed to one high power period in Test 2. Operation was terminated when fuel was consumed, yielding an overall fuel utilization of 97%.

The test was relatively free of problems, no corrosion or clogging was observed, and wall temperatures at full load conditions were uniform--similar to the results of Test 2. Actual condenser performance, however, was not as good as predicted, due to the continued presence of small amounts of noncondensable gas in the

system. The heat transfer coefficient of the condenser was calculated as described in Appendix A. It was found that the heat transfer coefficient on the condenser was lower than the expected value by a factor of 24. This strongly suggested that the design of the condenser area required improvement in order to achieve the full potential of the system.

#### 3.4 Test 4

In order to further control noncondensibles, a baffle was installed as shown in Figure 9. The baffle was designed to prevent an excessive pressure drop in the condenser.

When a baffle was not present, the vapor flow sweeps noncondensibles to the trapped area at light loads. For full load conditions, however, the primary vapor flow directly to the vapor surface competes with the flow to the trap and noncondensibles can collect along the wall. The baffle introduces a tangential vapor flow which now tends to sweep the wall clear of noncondensibles at full load, forcing the gases toward the trap where they do not impede condenser action.

The baffle worked as planned during the early portions of the test, pushing the noncondensibles to a narrow region near the trap. However, due to an excessively light construction, the baffle broke due to thermal cycling and failed during the latter portions of the test (this was observed as spread of the dark region uniformly around the combustor and from the condition of the baffle following the test).

In most other aspects, this test was similar to Test 3. Reasonably good fuel utilization was obtained, and the power density of the wick could be varied up and down over the range idle - 26.0 W/sq-cm. The operation of the heat pipe was not affected by fuel consumption until very near the end of the test.

While the vent on the noncondensable trap could be used satisfactorily in the early portion of the test, the line tended to become clogged with lithium as the test proceeded. This behavior indicated the need for some modification of the trap, if continued removal of noncondensable gases was desired throughout combustor operation.

### 3.5 Tests 5 and 6

These tests were run to examine capabilities for restarting the combustor. The trap was also modified by placing it in a horizontal position, in an attempt to reduce blockage of the vent line by condensed lithium, which was pumped to the top of the tube by natural convection instabilities when the vertical arrangement was used.

The first test, Test 5, was run for a period of three hours, over a variable load cycle, with two high-power periods, each one-half hour long, and then shut down as planned. The second test, Test 6, was a restart of the first test, after a storage period of three days. The combustor was operated for 1.3 hours during the second test and shut down upon indication of consumption of fuel due to increasing combustor pressure.

The overall fuel utilization for the two tests was in excess of 95%. The test series demonstrated the feasibility of restarting the reactive-heat-pipe-combustor.

Injector operation was satisfactory and no thermal cycling problems were encountered with the combustor materials. Noncondensable gas could be removed early in the period of operation from the vent in the gas collector. However, the small vent line eventually clogged with condensed lithium. Fortunately the remaining levels of noncondensibles were low, so that system operation could be undertaken at full power levels with the low levels of noncondensable gas remaining in the system stored in the volume of the trap. The flow of oxidizer did not introduce additional quantities of noncondensibles, in detectable amounts; which was true for all the tests. The interior components, wick, baffle, injector, etc., were in excellent condition following the test. No difficulty was encountered with failure of the baffle, due to its heavier construction for this test.

### 3.6 Discussion

The test series undertaken during this investigation demonstrated that the reactive-heat-pipe-combustor operates as anticipated. The major problem encountered during the tests, involved the presence of noncondensibles within the region of the condenser, which increased the heat transfer resistance. From the results of Test 5 and Test 6, the amount of noncondensibles can be controlled by properly degassing the fuel and the combustor walls; the remaining small amounts of noncondensibles can be controlled

by proper baffle design over the condenser and internal storage of noncondensibles in the ullage spaces of the combustor.

## CHAPTER IV

### THEORETICAL MODEL

Experimentation with a combustor having a specific configuration is of value for demonstrating the operation of the concept. However, this approach is limited in that it cannot consider all aspects of system design without excessive testing. Therefore, in the following, an analysis of the reactive-heat-pipe system is discussed, in order to study the general operating limitations of the concept over a wider range of variables than was accessible experimentally. In many ways, the system is similar to a heat pipe, and the present analysis has made liberal use of theoretical findings for heat pipes. New phenomena that must be considered involve reaction from one surface of the wick and the effect of the pressure difference across the wick.

The analysis addresses three potential failure modes as follows:

1. The wick can fail if it is unable to transfer sufficient lithium, to the top of the wick, for both reaction and heat transport requirements. Temperatures within the wick are maintained at acceptable levels, in the presence of reaction, by lithium evaporation from the surfaces of the wick. If fuel does not reach the upper portions of the wick, this region can reach high temperature levels where the material is directly attacked by the oxidizer, resulting in burn-out. This limit is referred to as the wick pumping limit.

2. The system will fail to operate as designed if the pressure within the reaction space is high enough to cause oxidizer to bubble under the lower edge of the wick. This can occur at high heat flux, where the temperature difference across the wick, and thus the pressure difference, is large. It is likely that the bubbles of gas would be reacted as they flow to the surface of the liquid [9], however, no experience has been obtained with operation at these conditions, and for the present this must be considered to be a failure mode. This limit is referred to as the liquid displacement limit.
3. The system will fail to operate as designed if there is an excessive temperature drop between the wick and the load. This results in excessive wick temperatures, potentially leading to failure. A variety of heat transfer limits are encountered, depending upon the design of the system, including: the thermal resistance of the wick, the vapor transport resistances, and the condensation resistance. The condensation process is also affected by the presence of noncondensibles, providing an allowable contamination limit.

A theoretical model which treats these aspects of the operation of a reactive-heat-pipe combustor is presented in the following.

#### 4.1 Wick Analysis

Figure 13 is a sketch of the wick configuration to be modelled, indicating the notation of the analysis. The wick has a length (H-L)

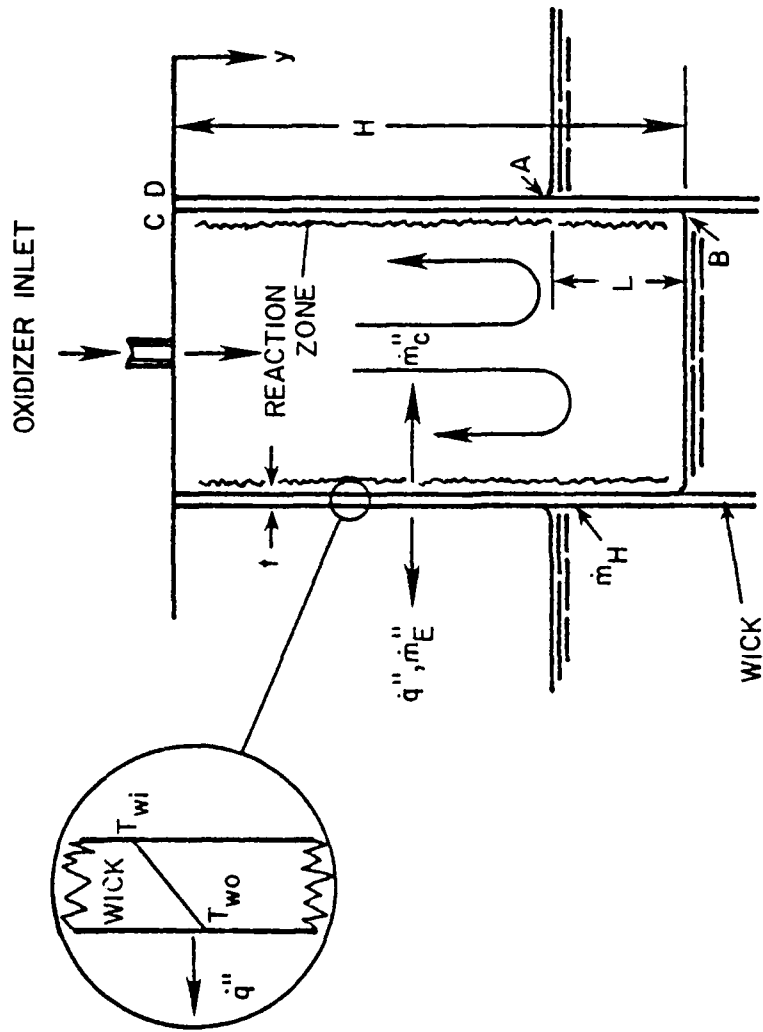


Figure 13 Sketch of the Wick Model

above the liquid surface. A liquid surface displacement  $L$  exists to compensate for the pressure difference across the wick.

In cases of laminar combustion with free convection, the rate of reaction is approximately proportional to the fourth root of wick length [10]. This is not a strong variation, and since the flow pattern within the reaction space of the combustor is not known, we assume that the burning rate of lithium is uniform over the wick surface. The rate of evaporation of lithium from the outside surface of the wick is also taken to be uniform. The system is assumed to be in a steady state condition and all the heat generated by reaction is assumed to be transferred through the wick, in the region above the liquid surface. The wick heat flux  $\dot{q}''$  is prescribed, since this parameter is a design variable.

These assumptions are conservative, since their effect is to increase the liquid pumping requirements of the wick. The circulation pattern within the reaction space is expected to cause the flow to pass upwards along the wick, so that the rate of reaction will be greater towards the bottom of the wick, reducing the height to which the reacting fuel must be pumped. Reaction energy produced toward the bottom of the wick, in the region  $H-L \leq y \leq H$ , is transferred directly to the bath, causing lithium to evaporate from the liquid surface. Since the analysis neglects this energy removal mechanism, the lithium flow for evaporation, and the temperature gradients in the wick, are somewhat overestimated.

The total mass flux of fuel for both combustion and evaporation, per unit exposed area of wick is

$$\dot{m}'' = \dot{m}''_E + \dot{m}''_C \quad (4.1)$$

Since the inside surface of the wick, of length  $L$ , also contributes to the reaction energy, these mass fluxes can be expressed in terms of the wick heat flux and the thermodynamic properties of lithium, as follows:

$$\dot{m}''_C = \frac{\dot{q}''}{Q_r} \left( \frac{H-L}{H} \right), \quad \dot{m}''_E = \frac{\dot{q}''}{h_{fg}} \quad (4.2)$$

The total lithium consumption per unit length along the lower circumference of the exposed portion of the wick is

$$\dot{m}'_{H-L} = (H-L)(\dot{m}''_C + \dot{m}''_E) \quad (4.3)$$

At typical combustor temperatures, the reaction energy of lithium and  $SF_6$  is 12.5 kW-hr/kg of lithium (4.75 kW-hr/kg of  $SF_6$  from Reference [3]). Since  $h_{fg}$  does not vary very much in the present temperature range, 1100-1300 K, the ratio of  $Q_r/h_{fg}$  can be taken as a constant. At 1200 K,  $h_{fg} = 20818 \text{ KJ/K}_g$  [11], yielding  $\alpha = Q_r/h_{fg} = 2.195$ .

Equation (4.3) can then be written

$$\dot{m}'_{H-L} = \frac{\dot{q}''H}{Q_r} [(1-\beta)(1+\alpha-\beta)] \quad (4.4)$$

where  $\beta = L/H$ .

The lithium flow in the wick varies in the vertical direction as follows

$$\dot{m}' = y\dot{m}'_{H-L}/(H-L) ; \quad H-L \geq y \geq 0 \quad (4.5)$$

The hydrostatic and viscous pressure drops within the wick are

provided by the capillary pumping force

$$\Delta p_S = \Delta p_B + \Delta p_V \quad (4.6)$$

To calculate the total viscous pressure loss, Darcy's Law is applied [12, 15, 16]

$$\frac{dp_V}{dy} = \frac{\mu_f \dot{m}' \pi D_W}{\rho_f K A_W} \quad (4.7)$$

The total viscous pressure drop is given by

$$\Delta p_V = \int_0^{H-L} dp_V \quad (4.8)$$

Substituting Equation (4.5) into Equation (4.7) and completing the integration yields

$$\Delta p_V = \frac{\mu_f H^2 (1-\beta)^2 \dot{q}''}{2\rho_f K t Q_r} (\alpha+1-\beta) \quad (4.9)$$

where

$$t = A_W / (\pi D_W)$$

Assuming constant liquid density, the hydrostatic pressure drop is

$$\Delta p_B = \rho_f g (H-L) \quad (4.10)$$

The capillary pumping force of the wick is [12, 15, 16]

$$p_S = 2 \left( \frac{1}{R_C} - \frac{1}{R_A} \right) \quad (4.11)$$

Since the meniscus radius at position B is always infinitely large, we get  $\rho_f g L = \frac{2\sigma}{R_A}$  and we can write Equation (4.11) as follows

$$\Delta p_S = \frac{2\sigma}{R_C} - \rho_f g L \quad (4.12)$$

The capillary pumping force,  $\Delta p_S$ , can have its maximum value when  $R_C$  reaches its minimum value. This occurs when [14]

$$R_C = R_m = (\delta + d')/2 \quad (4.13)$$

At the maximum pumping height condition, the maximum capillary force just balances the hydrostatic and viscous pressure loss, yielding

$$\frac{2\sigma}{R_m} = \rho_f g H + \dot{q}'' X H^2 \quad (4.14)$$

where

$$X = \frac{\mu_f (1-\beta)^2}{2\rho_f K t Q_r} (\alpha + 1 - \beta)$$

Solving for the maximum pumping height, we obtain

$$H_{\max} = \frac{-\rho_f g + \left[ \rho_f^2 g^2 + 4\dot{q}'' X \left( \frac{2\sigma}{R_m} \right) \right]^{1/2}}{2X\dot{q}''} \quad (4.15)$$

If  $H$  is specified, the maximum heat flux is given by Equation (4.14)

$$\dot{q}''_{\max} = \frac{2\sigma/R_m - \rho_f g H}{X H^2} \quad (4.16)$$

The permeability of the wick can be calculated from [17]

$$K = d'^2 \epsilon'^3 / [122(1-\epsilon')^2] \quad (4.17)$$

where

$$\epsilon' = 1 - (\pi F N d' / 4) \quad (4.18)$$

The crimping factor,  $F$ , has a value of 1.05 [17].

In order to calculate  $H_{\max}$ , we have to know the value of  $L$  in  $\beta$ .  $L$  can be determined by noting that the liquid head must equal the pressure difference across the wick.

$$P_{wi} - P_{wo} = \rho g_f L \quad (4.19)$$

The temperature drop through the wick is

$$\dot{q}'' = k_w (T_{wi} - T_{wo}) / t \quad (4.20)$$

where  $k_w$  is the effective thermal conductivity of the wick. This parameter is determined as follows [12]

$$k_w = (\beta' - \epsilon) k_f / (\beta' + \epsilon) \quad (4.21)$$

where

$$\beta' = (k_f + k_s) / (k_f - k_s)$$

and  $\epsilon$  is the volume fraction of the solid phase.

The temperature jump due to evaporation results from nonequilibrium at the liquid surface, and can be represented as follows [13]

$$j = \left( \frac{\bar{M}}{2\pi R} \right)^{1/2} \left[ \sigma_e \frac{p_{wo}}{T_{wo}^{1/2}} - \sigma_c (1-a\pi^{1/2}) \frac{p_g}{T_g^{1/2}} \right] \quad (4.22)$$

where  $a = \frac{u}{(2RT_g/\bar{M})^{1/2}}$  represents the ratio of the bulk vapor velocity to a characteristic molecular velocity. Equation (4.22) results from the assumption that  $a$  is very small, due to large heat of evaporation of lithium; and also neglects the effect of the mean velocity of liquid molecules at the phase interface [19]. Since  $\sigma_e = \sigma_c = 1.0$  [20], Equation (4.22) becomes

$$j = \left( \frac{2\bar{M}}{\pi R} \right)^{1/2} \left( \frac{p_{wo}}{T_{wo}^{1/2}} - \frac{p_g}{T_g^{1/2}} \right) \quad (4.23)$$

The saturated vapor pressure of lithium can be represented as [18]

$$p = \exp[A - (B/T)] \quad (4.24)$$

Knowing the temperature of the inner surface of the wick and the temperature after the evaporation jump, provides the following expression for the liquid displacement

$$L = \frac{1}{\rho_f g} \{ \exp[A - B(1/T_{wi} + H/T_g)] (\exp[B/T_g] - \exp[B/T_{wi}]) \} \quad (4.25)$$

As long as we know  $L$ , by trial and error we can calculate  $H_{\max}$  from Equation (4.15). If  $H$  is fixed, we can calculate the  $\dot{q}_{\max}''$  by trial and error from Equations (4.16), (4.20), (4.23), and (4.25). When the heat flux  $\dot{q}''$  is small,  $\beta$  can be set equal to zero without a large error, yielding a straightforward calculation. The

thermophysical properties required in the calculation are discussed in Section 4.4.

#### 4.2 Transport Tube Analysis

In order to simplify the analysis, the flow of vapor to the condenser and the condensation process itself were considered independently, although in many configurations flow and condensation occur at the same time, e.g., in the baffled condenser used in Tests 4-6. The model under this assumption is illustrated in Figure 14. Flow process is taken to be adiabatic with friction, with the vapor entering the passage without any loss. The gas adjacent to the condenser surface is taken to be "well mixed" so that the concentration of noncondensable gas is uniform over the surface of the condenser.

The transport system is composed of a converging nozzle and a tube with constant friction factor and constant cross-sectional area. Adiabatic vapor flow in the tube is assumed. Since the bulk vapor velocity leaving the wick is relatively small, e.g., 0.8 m/sec at 1000 kW/m<sup>2</sup> wick heat flux and 1200 K, we can reasonably assume that the vapor in the chamber is at rest without much error. We also assume that the acceleration process in the inlet nozzle is isentropic, and any pressure recovery as the flow enters the condenser area is neglected. The required pressure ratio of the inlet and outlet of the nozzle is given implicitly as follows [21]

$$\frac{\dot{Q}}{h_{fg} A_t p_o} \left( \frac{(\gamma-1)RT_o}{2\gamma\bar{M}} \right)^{1/2} = \left( \frac{p_i}{p_o} \right)^{1/\gamma} \left[ 1 - \left( \frac{p_i}{p_o} \right)^{\gamma-1/\gamma} \right]^{1/2} \quad (4.26)$$

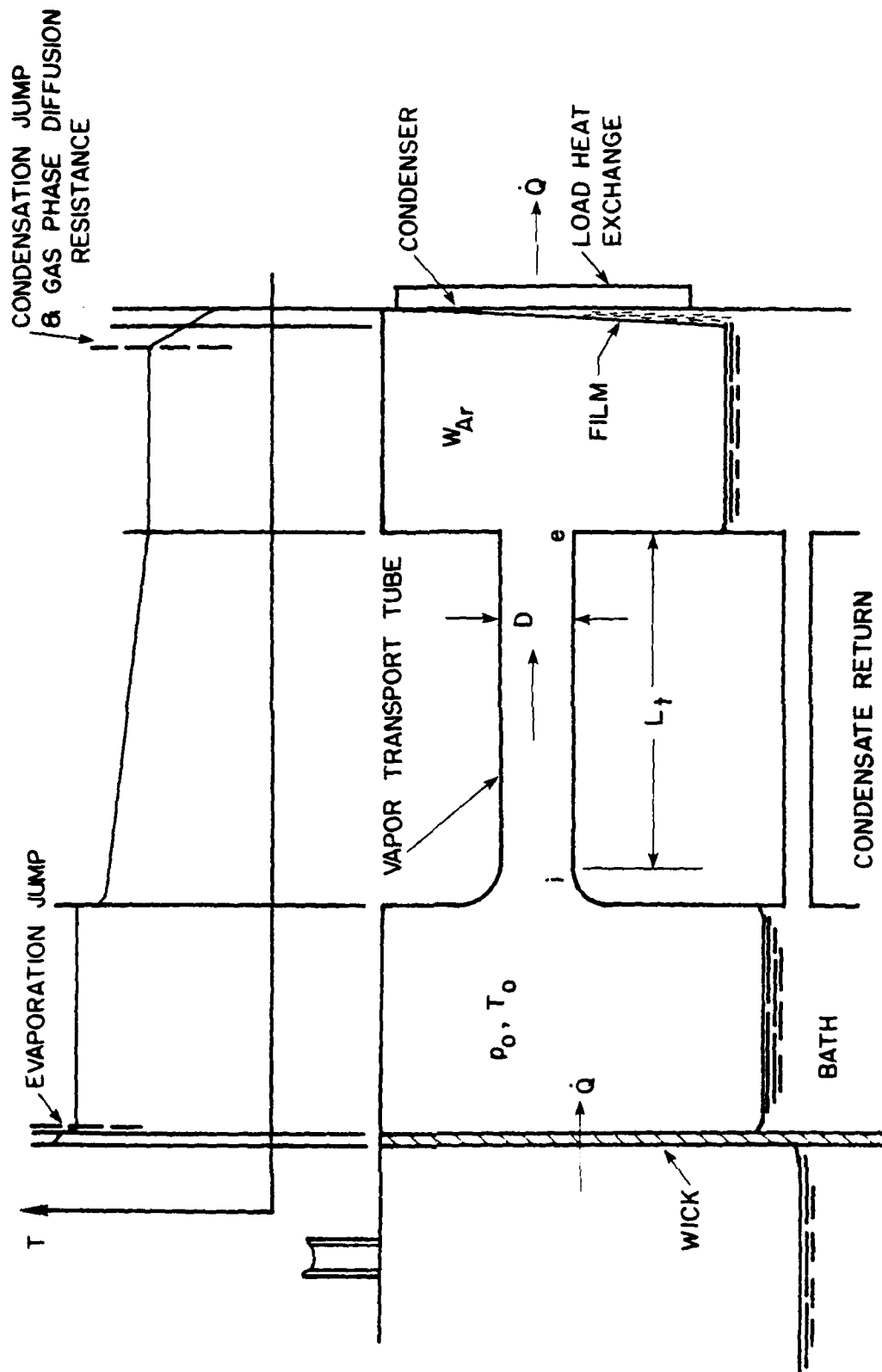


Figure 14 Model of the Heat Transport System

The Mach number and the temperature at the inlet of the constant area section is then given by

$$M_i = \left( \frac{2}{\gamma-1} \right)^{1/2} \left[ \left( \frac{p_i}{p_o} \right)^{1-\gamma/\gamma} - 1 \right]^{1/2} \quad (4.27)$$

$$T_i = T_o / [1 + (\gamma-1)M_i^2/2] \quad (4.28)$$

The Mach number at the outlet of the transport tube is determined from [21]

$$\frac{fL_t}{D} = \frac{1}{\gamma} \left( \frac{1}{M_i^2} - \frac{1}{M_e^2} \right) + \left( \frac{\gamma+1}{2\gamma} \right) \ln \left( \frac{M_i^2 T_i}{M_e^2 T_e} \right) \quad (4.29)$$

and the pressure ratio and temperature ratio across the tube are

$$\frac{T_e}{T_i} = \frac{1+(\gamma-1)M_i^2/2}{1+(\gamma-1)M_e^2/2} \quad (4.30)$$

$$\frac{p_e}{p_i} = \frac{M_i}{M_e} \left[ \frac{1+(\gamma-1)M_i^2/2}{1+(\gamma-1)M_e^2/2} \right]^{1/2} \quad (4.31)$$

Given the inlet conditions to the transport tube, and the heat flow per unit area, Equation (4.26) can be solved to yield  $p_i/p_o$ . Substituting the value of  $p_i/p_o$  into Equations (4.27) and (4.28), then provides the Mach number and temperature at state i. The quantity  $fL_t/D$  is taken as a parameter in the analysis, knowing this quantity and the conditions at state i, simultaneous solution of Equations (4.29) and (4.30) yields the Mach number and temperature ratio at the exit of the tube. Equation (4.31) finally provides the condenser pressure.

As long as the flow is not sonic at the exit of the transport tube, solution of Equations (4.26)-(4.31) yields the pressure in the region adjacent to the condenser [21]. If the flow is choked, the pressure in the condenser region is determined by the cooling characteristics of the condenser and there is a pressure discontinuity at the exit of the transporting tube. The choked condition is defined by  $M_e = 1$ , and the corresponding inlet Mach number is given implicitly by

$$\frac{fL_t}{D} = \frac{1}{\gamma} \left( \frac{1}{M_i^2} - 1 \right) + \left( \frac{\gamma+1}{2\gamma} \right) \ln \frac{(\gamma+1)M_i^2/2}{1+(\gamma-1)M_i^2/2} \quad (4.32)$$

In order to return the condensate in the condenser space to the combustor chamber, a certain pressure head must be applied to the condensate to compensate for the pressure difference between the combustion chamber, and the viscous loss in the return tube. The loss in the return tube can be calculated by conventional methods.

### 4.3 Condenser Analysis

4.3.1 Condensation in the Absence of Noncondensibles. If there is no noncondensable gas in the condenser, the thermal resistances from the vapor space to the inner surface of the condenser are the resistance of the condensate film on the heat exchanger surface, and the interfacial resistance between the vapor and liquid film.

For the liquid film, we assume that subcooling of the condensate may be neglected due to the high thermal conductivity of liquid lithium. The temperature variation is illustrated schematically in Figure 15. The condensation resistance due to the

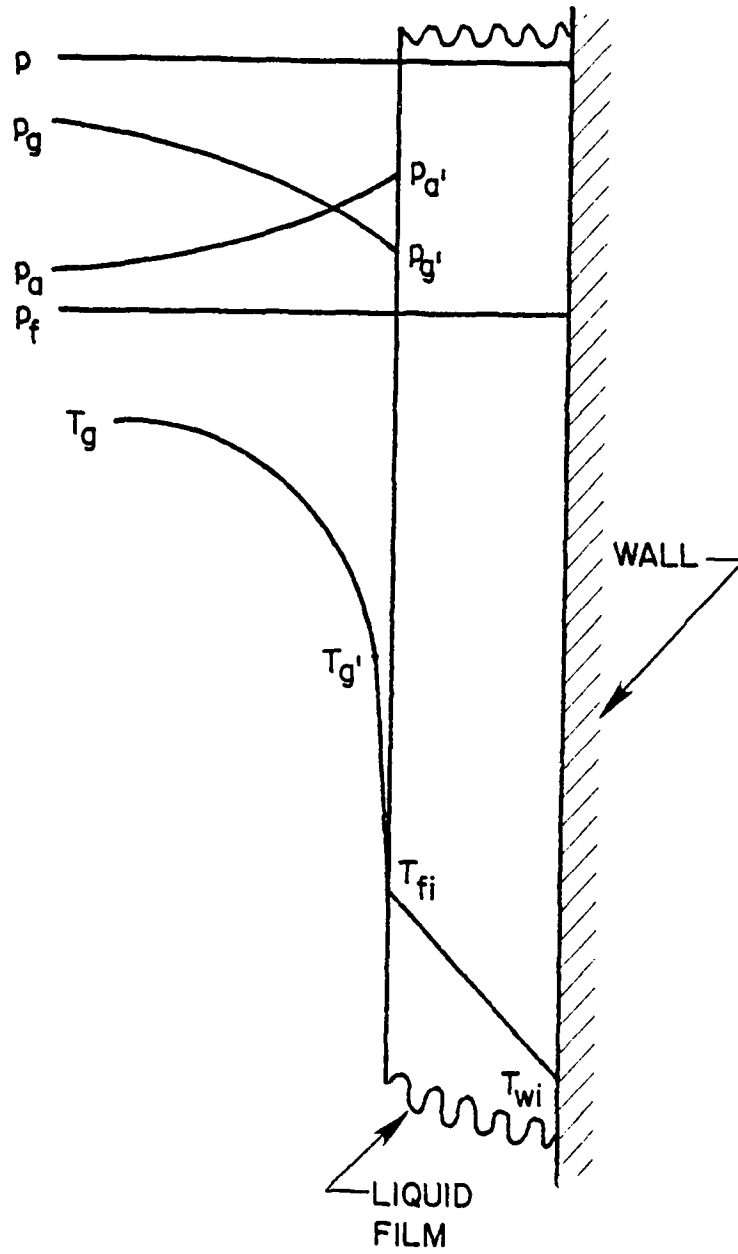


Figure 15 Condensation Resistances

liquid film is [27]

$$\frac{\dot{q}_c''}{T_{fi} - T_{wi}} = 1.13 \left[ \frac{g \rho_f (\rho_f - \rho_g) k_f^3 h_{fg}}{L_c \mu_f (T_{fi} - T_{wi})} \right]^{1/4} \quad (4.33)$$

In Equation (4.33), a correction factor of 1.2 [27] is used to modify the theoretical value for the effect of the downward flowing vapor in reducing the thickness of the condensate film and the mixing action of ripples in this film. This correlation is based on the evaluation of the properties at the mean film temperature

$(T_{fi} + T_{wi})/2$ , while the latent heat  $h_{fg}$  is to be taken at  $T_{fi}$  [28].

If the film is turbulent, then

$$\frac{\dot{q}_c''}{T_{fi} - T_{wi}} = 0.0134 \left( \frac{k_f^3 \rho_f^2 g}{\mu_f^2} \right)^{1/3} \left( \frac{\rho_f^2 g L_c^3}{3 \mu_f^2} \right)^{0.4} \quad (4.34)$$

For the cases considered, the film is always in a laminar region.

Considering the extreme case,  $\dot{q}_c'' = 1000 \text{ KW/m}^2$  and  $T_{wi} = 1400 \text{ K}$ , the film is laminar when  $L_c$  is below 0.6m.

The interfacial resistance is essentially the reciprocal of the evaporative resistance [13]

$$\frac{\dot{q}_c''}{h_{fg}} = \left[ \frac{2\bar{M}}{\pi R} \right]^{1/2} \left[ \frac{p_{g'}}{T_{g'}^{1/2}} - \frac{p_{fi}}{T_{fi}^{1/2}} \right] \quad (4.35)$$

where pressures are related to the temperatures through

$$p = \exp[A - (B/T)] \quad .$$

4.3.2 Condensation in the Presence of Noncondensibles. When a noncondensable gas is present, there is a gas film adjacent to the liquid film. The heat transfer across the gas film is the sum of the sensible heat transferred across the layer and the heat of vaporization of lithium vapor that diffuses across the layer and condenses on the liquid film. The basic equation for the gas film is

$$\dot{q}_c'' = h(T_g - T_{g'}) + K_g \bar{M}_{fg} (p_g - p_{g'}) \quad (4.36)$$

If no forced convection is present, the convective effect is measured by the Grashof number

$$G_r = g L_c^3 (\rho_{g'} - \rho_g) / \rho_g \nu^2 \quad (4.37)$$

The mass transfer coefficient is given by [22]

$$\frac{K_g L_c RT}{D_{Li-Ar} p} \frac{p_{am}}{p} = 1.02 (Gr \cdot Sc)^{0.373} \quad (4.38)$$

for  $10^3 < Gr < 10^7$ . In this equation,  $p_{am}$  is the logarithmic mean of the partial pressures of noncondensable gas at the interface and in the bulk mixture,

$$p_{am} = (p_g - p_{g'}) / \ln[(p - p_{g'}) / (p - p_g)] \quad (4.39)$$

The sensible heat transfer coefficient is obtained from [28]

$$\frac{h L_c}{K_g} = 0.55 (Gr \cdot Pr)^{0.25} \quad (4.40)$$

for  $10^4 < Gr Pr < 10^9$ . Since the rate of mass transfer is less than

$0.05 \text{ kg/m}^2\text{s}$ , when the heat flux in the condenser is  $1000 \text{ kW/m}^2$ , we can simply use the coefficient given in Equation (4.40) without introducing much error due to the bulk mass transport effect [13].

Since interfacial conditions are not known, Equations (4.36)-(4.40) must be solved by trial and error. The properties of gas mixtures used in the calculation are summarized in Appendix A.

Since the pressure recovery of the flow leaving the transport tube has been neglected, the vapor in the gas space adjacent to the condenser is somewhat superheated. Since the enthalpy of superheating is small compared to  $h_{fg}$ , however, this contribution has been neglected. Superheating improves heat transfer characteristics [23], therefore, neglecting this phenomenon makes the present calculations somewhat conservative.

#### 4.4 Thermophysical Properties

The properties of lithium and argon are mainly selected from References [11, 18]. Although the reported properties are not quite the same for these two sources, the discrepancies are not large over the present range of calculations. The atomic weights, melting points, boiling points, and critical points of lithium and argon are summarized in Table 3.

4.4.1 Properties of Lithium. The detailed properties of lithium are presented in Table 4 [11]. For convenience in the calculations the properties of liquid lithium can be correlated by the following relation [18]

Table 3

Molecular Weight, Melting Point, Boiling Point and  
Critical Point of Argon and Lithium

Quantity	Lithium	Argon
Atomic Weight (kg/kg-mole)	6.940	39.944
Melting Point (*K)	453.7	83.78
Boiling Point at 760 mm Hg (*K)	1615	87.29
Critical Temperature (*K)	3800	150.86
Critical Pressure (bar)	970	50
Density at Critical Point (kg/m <sup>3</sup> )	100	536

Table 4

## Thermophysical Properties of Lithium at Saturation Conditions

Temperature K	Latent Heat KJ/kg	Vapor		Liquid		Vapor		Liquid	
		Molecular Weight	Density kg/m <sup>3</sup>	Density kg/m <sup>3</sup>	Thermal Conductivity W/m-K	Thermal Conductivity w/m-K	Thermal Conductivity w/m-K	Viscosity (x 10 <sup>3</sup> ) N-s/m <sup>2</sup>	
1000	21471	7.119	463	8.213x10 <sup>-5</sup>	55.2	--	--	0.247	
1050	21317	7.162	457	1.886x10 <sup>-4</sup>	--	--	--	--	
1100	21156	7.209	452	4.010x10 <sup>-4</sup>	57.6	120	120	0.225	
1150	20989	7.260	447	7.973x10 <sup>-4</sup>	--	--	--	--	
1200	20818	7.313	442	1.494x10 <sup>-3</sup>	59.8	138	138	0.207	
1250	20644	7.368	437	2.658x10 <sup>-3</sup>	--	--	--	--	
1300	20466	7.425	432	4.319x10 <sup>-3</sup>	62.1	156	156	0.192	
1350	20288	7.483	427	7.380x10 <sup>-3</sup>	--	--	--	--	
1400	20110	7.541	422	1.162x10 <sup>-2</sup>	--	172	172	0.180	

Table 4 (Continued)

Temperature K	Vapor Viscosity ( $\times 10^7$ ) N-s/m <sup>2</sup>	Liquid Specific Heat (Cp) KJ/kg-K	Vapor Specific Heat (Cp) KJ/kg-K	Liquid Surface* Tension N/m	Vapor Pressure bar
1000	--	4.16	8.171	0.321	$9.598 \times 10^{-4}$
1050	--	4.16	8.685	--	$2.301 \times 10^{-3}$
1100	--	4.15	9.114	0.307	$5.090 \times 10^{-3}$
1150	--	4.15	9.465	--	$1.051 \times 10^{-2}$
1200	--	4.14	9.723	0.293	$2.04 \times 10^{-2}$
1250	--	4.15	9.905	--	$3.752 \times 10^{-2}$
1300	129	4.16	10.019	0.279	$6.583 \times 10^{-2}$
1350	--	4.17	10.066	--	0.1108
1400	140	4.19	10.049	0.265	0.1794

\*Interpolation in Reference [11].

$$\rho = 562 - 0.1 T \quad (4.41)$$

$$\sigma = 0.447 - 1.07 \times 10^{-4} T - 1.351 \times 10^{-8} T^2 \quad (4.42)$$

$$k = 21.874 + 0.056255 T - 1.9325 \times 10^{-5} T^2 \quad (4.43)$$

$$p = \exp [23.06 - 18569.20/T] \quad (4.44)$$

$$\mu = \exp [-7.09 + 132.70/T - 1.190 \times 10^{-3} T] \quad (4.45)$$

where  $T$  is in K,  $\rho$  in  $\text{kg/m}^3$ ,  $\sigma$  in N/m,  $k$  in W/mK,  $p$  in  $\text{N/m}^2$  and  $\mu$  in  $\text{Ns/m}^2$ .

Since similar correlations for lithium vapor are not available, the data in Reference [11] was correlated to obtain the following formulas for saturated liquid lithium vapor.

$$\bar{M}_{\text{Li}} = \exp [2.02 - 1.4 \times 10^{-4} (1400-T)] \quad (4.46)$$

$$\log_{10} \rho = -49.052 + 14.988 \log_{10} (-589 + 2.0275 T - 4.375 \times 10^{-4} T^2) \quad (4.47)$$

$$k = 5.641 \times 10^{-2} T^{1/2} - 6.28 \times 10^{-4} T - 1.05975 \quad (4.48)$$

$$\mu = 1.29 \times 10^{-5} + 10^{-8} \times (T-1300) \quad (4.49)$$

The temperature ranges for the above correlations are summarized in Table 5.

4.4.2 Properties of Argon. From the data of Reference [11], it is found that most of the properties of argon, except density, are not sensitive to pressure changes. For example, the viscosity at 900 K changes only about one percent when the pressure is changed

Table 5

## Reliable Temperature Ranges of the Correlations for Lithium Properties

Properties	$\bar{M}_g$	$\rho_f$	$\rho_g$	$\sigma_f$	$k_f$	$k_g^*$	$\mu_f$	$\mu_g^*$	P
Lower Bound, K	800	500	900	460	453.6	1100	500	1300	453.7
Upper Bound, K	2000	2000	1600	1500	1300	2000	1500	2000	1900

\*No data are available below their lower bounds.

from 1 to 80 bar. Therefore, the properties of argon are approximated by the values at a pressure of 1 bar, and are presented in Table 6 [11]. The thermal conductivity of argon in the range 1000-1400 K, at 1 bar, can be correlated by the following equation

$$k = 4.76 \times 10^{-2} + 2.6 \times 10^{-5} (T - 1150) \quad (4.50)$$

and the viscosity in the range of 1000-1500 K at 1 bar can be correlated by

$$\mu = 6.679 \times 10^{-5} + 3.5 \times 10^{-8} (T - 1300) \quad (4.51)$$

Table 6

## Thermophysical Properties of Argon at Pressure of 1 Bar

Temperature K	Thermoconductivity ( $\times 10^3$ ) W/m-K	Viscosity ( $\times 10^7$ ) Ns/m <sup>2</sup>	Specific Heat (Cp) KJ/kg-K
1000	43.6	560.0	0.52
1050	45.0	--	0.52
1100	46.3	598.0	0.52
1150	47.6	--	0.52
1200	48.9	633.7	0.52
1250	50.2	651.2	0.52
1300	51.4	667.9	0.52
1350	52.6	--	0.52
1400	53.7	700.9	0.52

## CHAPTER V

### RESULTS

The analytical results for the wick, and for the vapor transporting and condensation process, will be discussed separately. This will be followed by consideration of the complete system for some typical conditions.

#### 5.1 Wick

Two thermal resistances are considered here, the wick itself and the evaporative interface. Figure 16 is an illustration of the heat transfer characteristics of a wick consisting of two layers of 100-mesh screen, which is the arrangement employed in the tests. The total temperature drop increases almost linearly with increasing heat flux. Since the thermal conductivity of liquid lithium varies slightly with temperature, the resistance of the wick is relatively independent of temperature. The evaporative resistance increases as the mean temperature level decreases.

As shown in Figures 17 and 18, increasing the number of layers of screen, and reducing the mesh size, increases the thermal resistance of the wick, however, the evaporative resistance only depends on the mean temperature level and the heat flux. The linear relationship between the temperature difference and the wick heat flux is also valid in Figures 17 and 18. The wider range of the temperature difference can be conveniently plotted with a semi-logarithmic scale.

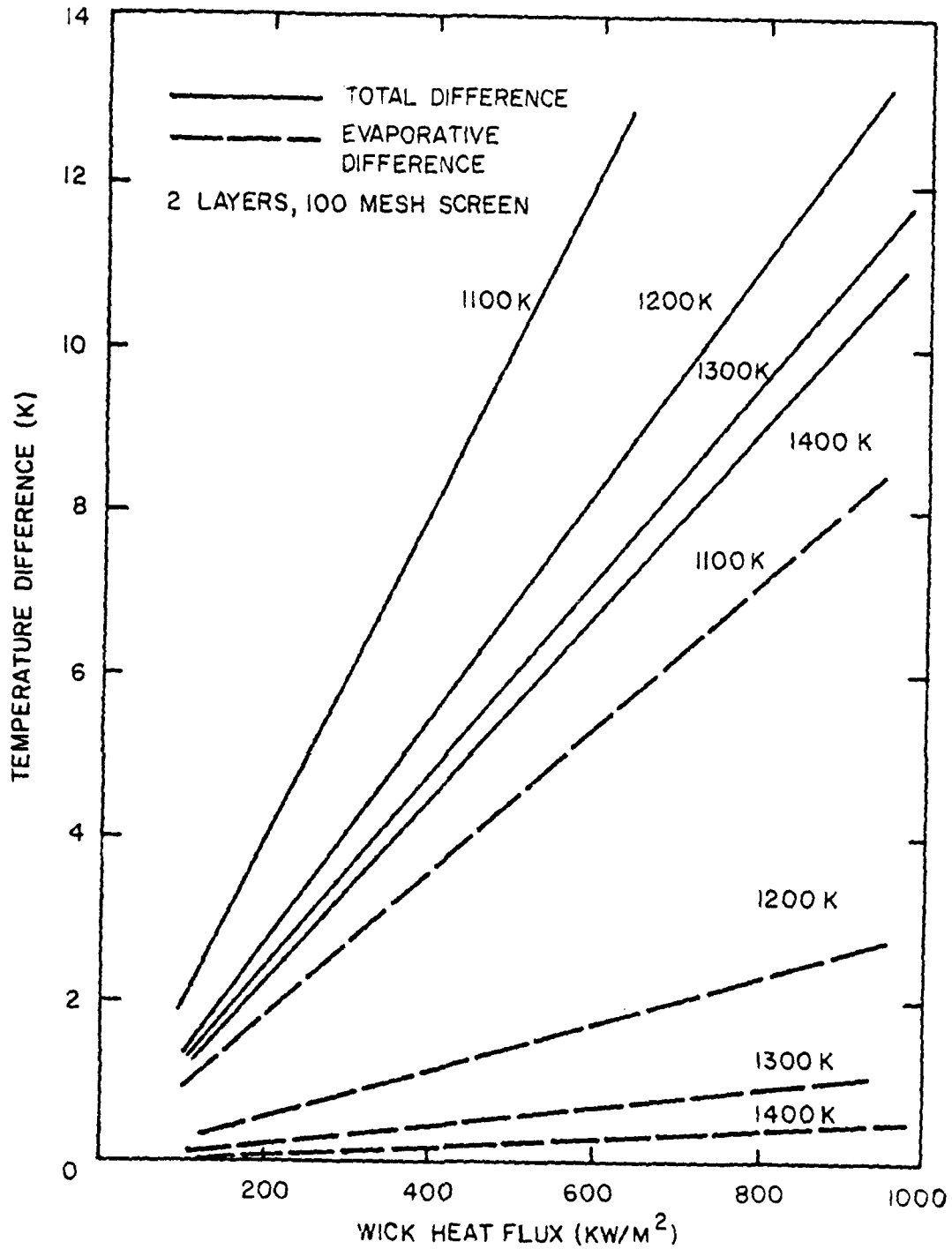


Figure 16 Wick Thermal Resistance

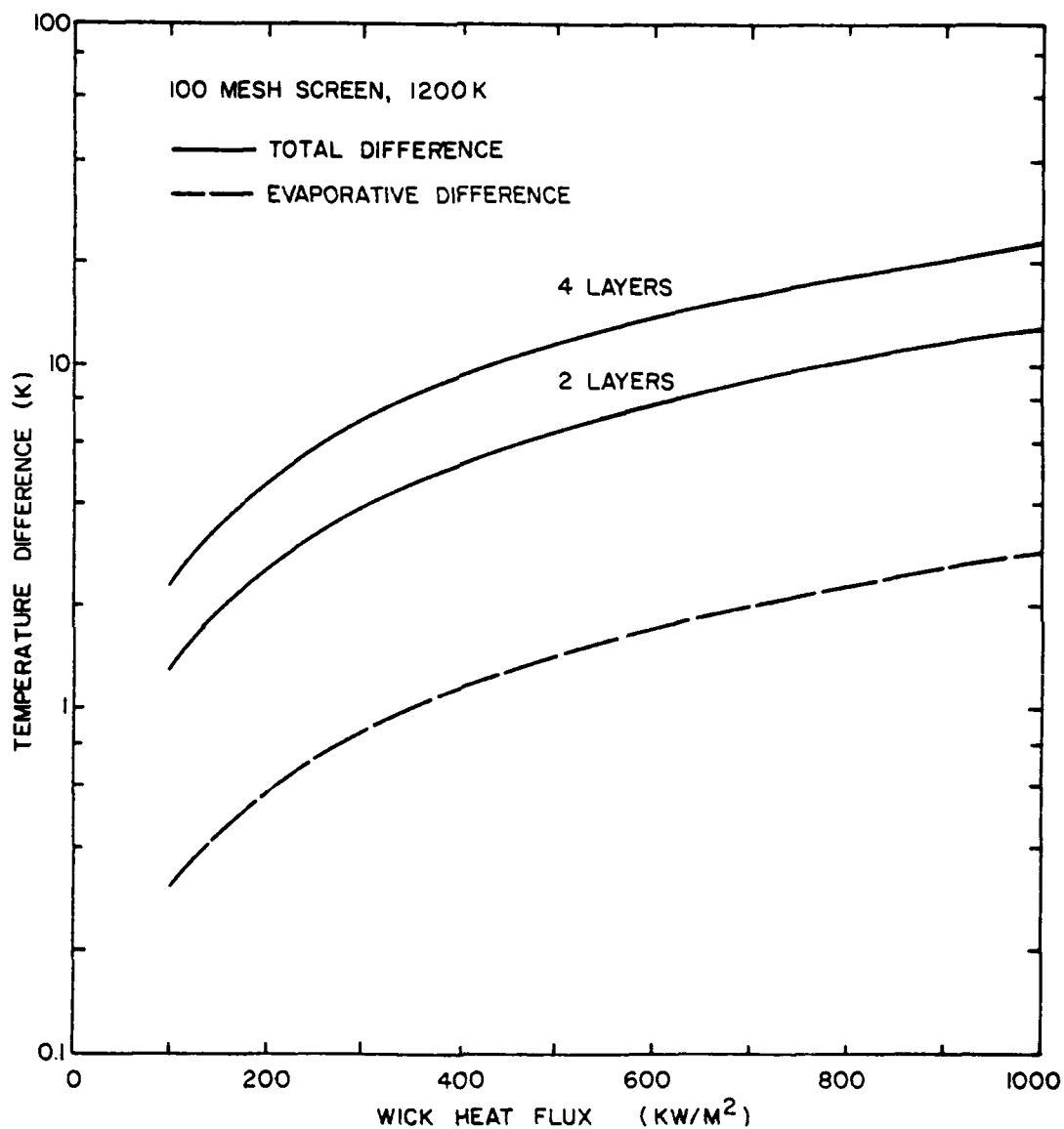


Figure 17 Wick Thermal Resistance with Different Layers of Screen

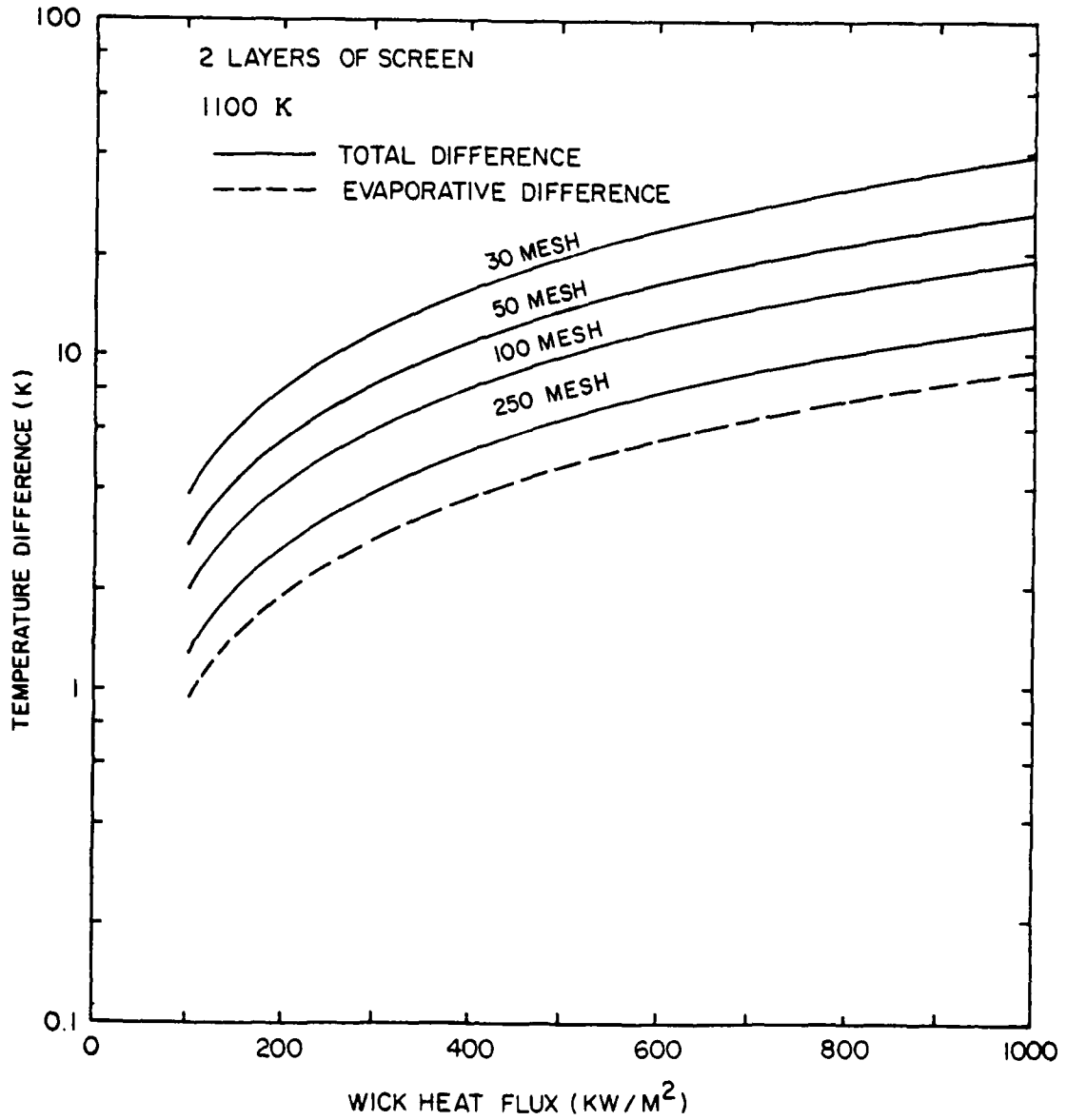


Figure 18 Wick Thermal Resistance with Different Mesh Sizes

Increasing the mesh will increase the capillary ability of the wick, but it will also increase the viscous loss. Therefore, there is an optimum mesh for any given operating condition. Figure 19 is an illustration of the pumping height,  $H$ , and the net pumping height  $H-L$ , for various mesh sizes for heat fluxes of 100 and 1000  $\text{kW/m}^2$ , at 1200 K. We can see that the maximum pumping height occurs for approximately a 75 mesh wick, under the specified conditions.

Figures 20 and 21 are illustrations of the variation of pumping height and net pumping height as a function of heat flux, with temperature as a parameter for mesh size. The net pumping height always decreases with increasing heat flux, and is generally lower at higher operating temperatures. The pumping height itself reaches a minimum with increasing heat flux, and is generally higher at higher temperatures. The minimum occurs since  $L$  becomes larger at higher heat fluxes, reducing the height that the lithium must be pumped through the exposed portion of the wick, which compensates for the increased lithium flow rate. The temperature effect results from the reduced density of lithium at higher temperatures, which also increases  $L$  and reduces pumping requirements in the exposed portion of the wick.

The net pumping heights illustrated in Figures 19-21, are relatively small, which limits the flexibility of design since reasonable wick heights can be necessary to provide sufficient reaction area within a given volume. Larger net pumping heights can be obtained by employing an arterial wick. In this case, the

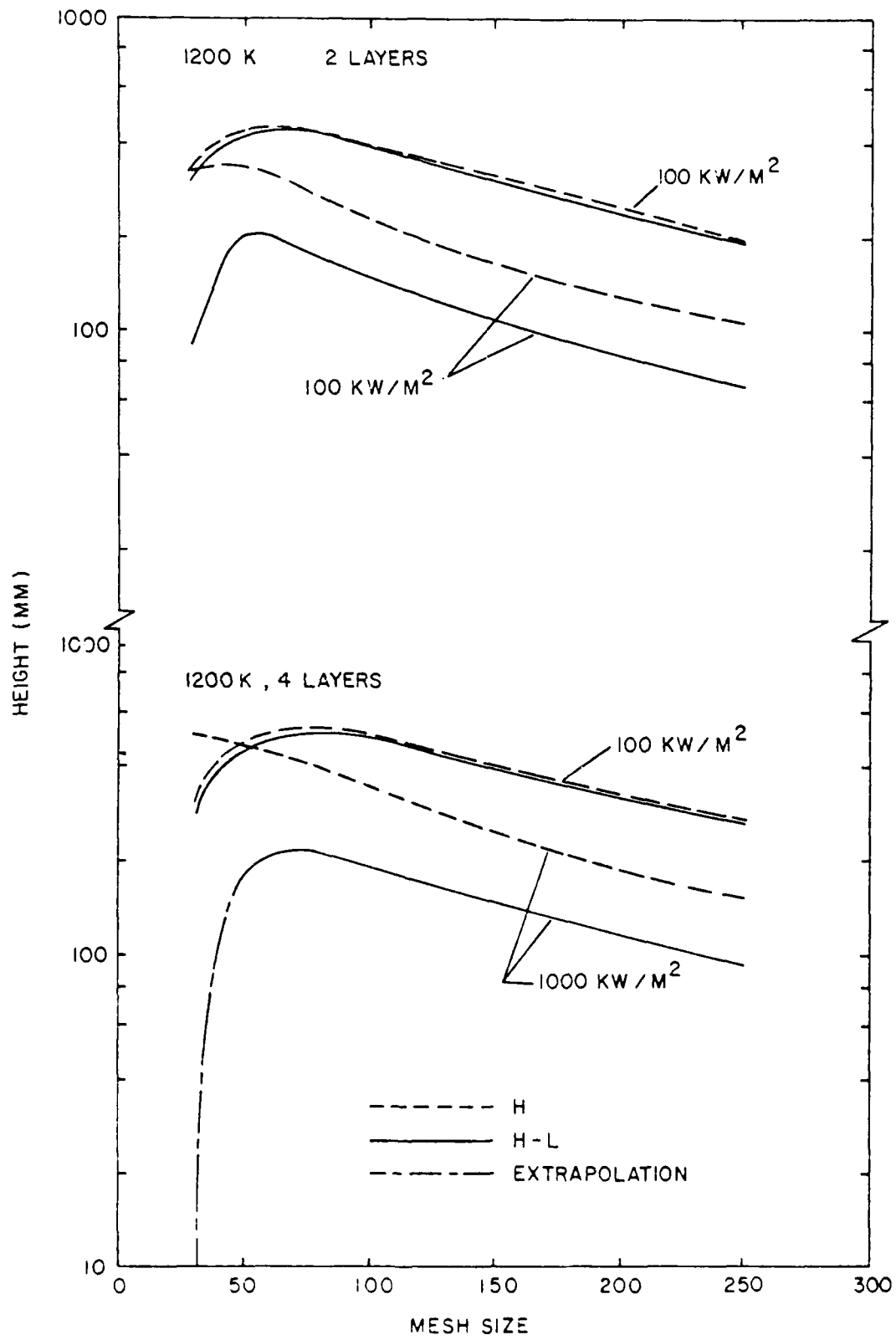


Figure 19 Wick Pumping Heights for Different Mesh Sizes

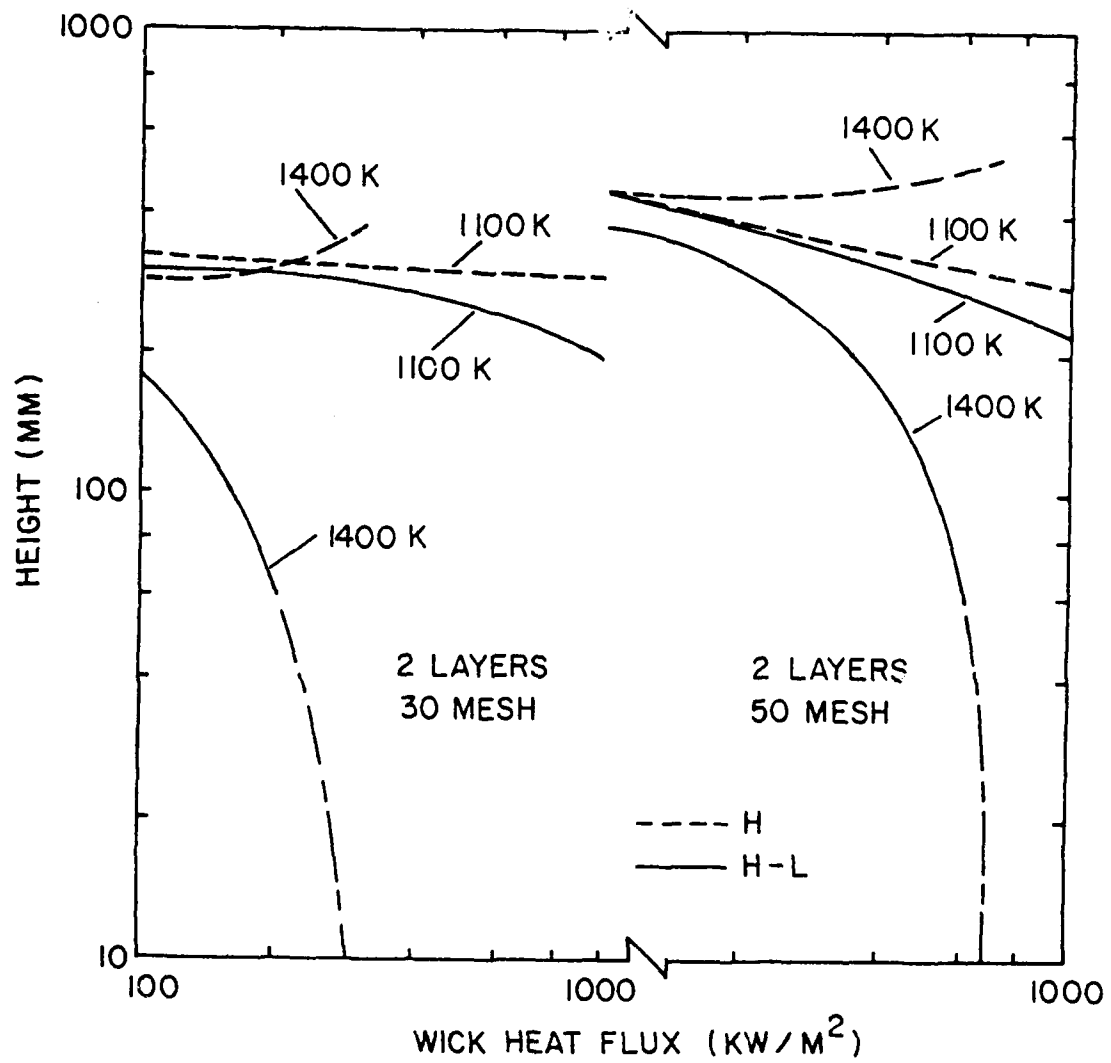


Figure 20 Wick Pumping Heights for Different Temperatures

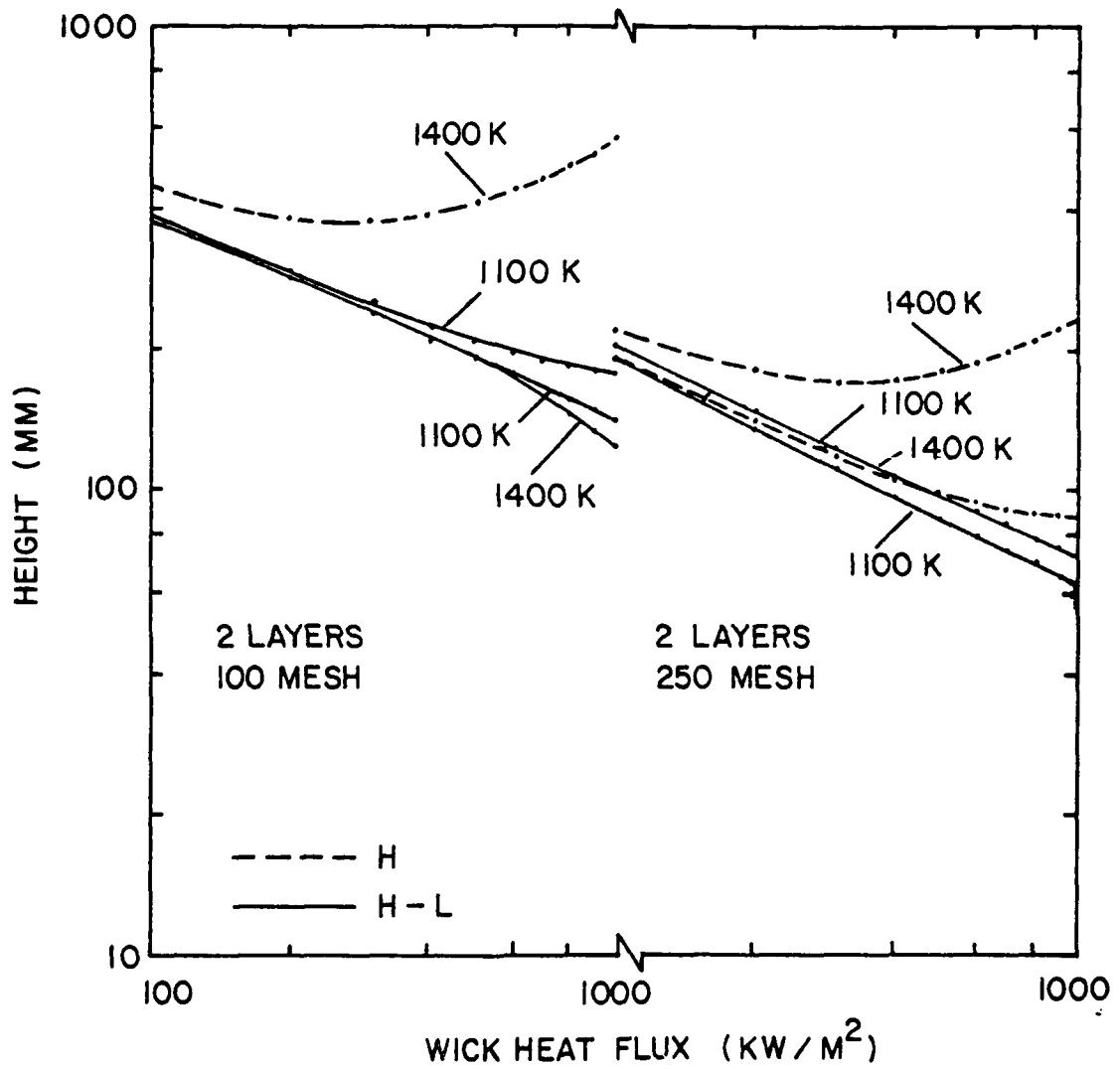


Figure 21 Wick Pumping Heights for Different Temperatures

liquid flows through an independent tube, and is not just confined to the cross-section of the wick. Only the final distribution of the liquid across the region between arteries occurs within the wick itself. In this case, the viscous pressure drop in the wick can be made much smaller than in the conventional wick arrangement, which increases the net pumping height.

Table 7 summarizes the pumping heights for four different mesh sizes using an arterial wick. When an arterial wick is used, finer mesh screen is favored, and the pumping height is independent of the heat flux. The pumping heights are also substantially greater than the results shown in Figure 19, where the liquid flow is confined to the wick cross-section.

## 5.2 Vapor Transport and Condensation

The losses in this section include the vapor flow resistance and resistances in the condenser. The condenser resistance involves the resistance of the film, the resistance at the interface, and the resistance of diffusion through any noncondensable gas layer. In order to highlight losses in the vapor transport tube, the area of the condenser is taken to be ten times larger than that of the wick, while the vapor transport tube is taken to be only .1 that of the wick. In order to fix ideas, the combustor geometry used in the tests employed  $A_t/A_w = 0.23$ ; and  $fL/D$  in the range 0-10, depending upon operation conditions and the appropriate selection of transport tube length (in view of the fact that vapor flow and condensation occur simultaneously in a portion of the arrangement the length can only be approximated). Figure 22 is an illustration of a portion of the

Table 7

 $H_{\max}$  for Arterial Wicks (mm)

Mesh Size	Temperature (K)		
	1100	1250	1400
30 x 30	334	322	309
50 x 50	556	537	515
100 x 100	1113	1074	1031
250 x 250	2782	2685	2577

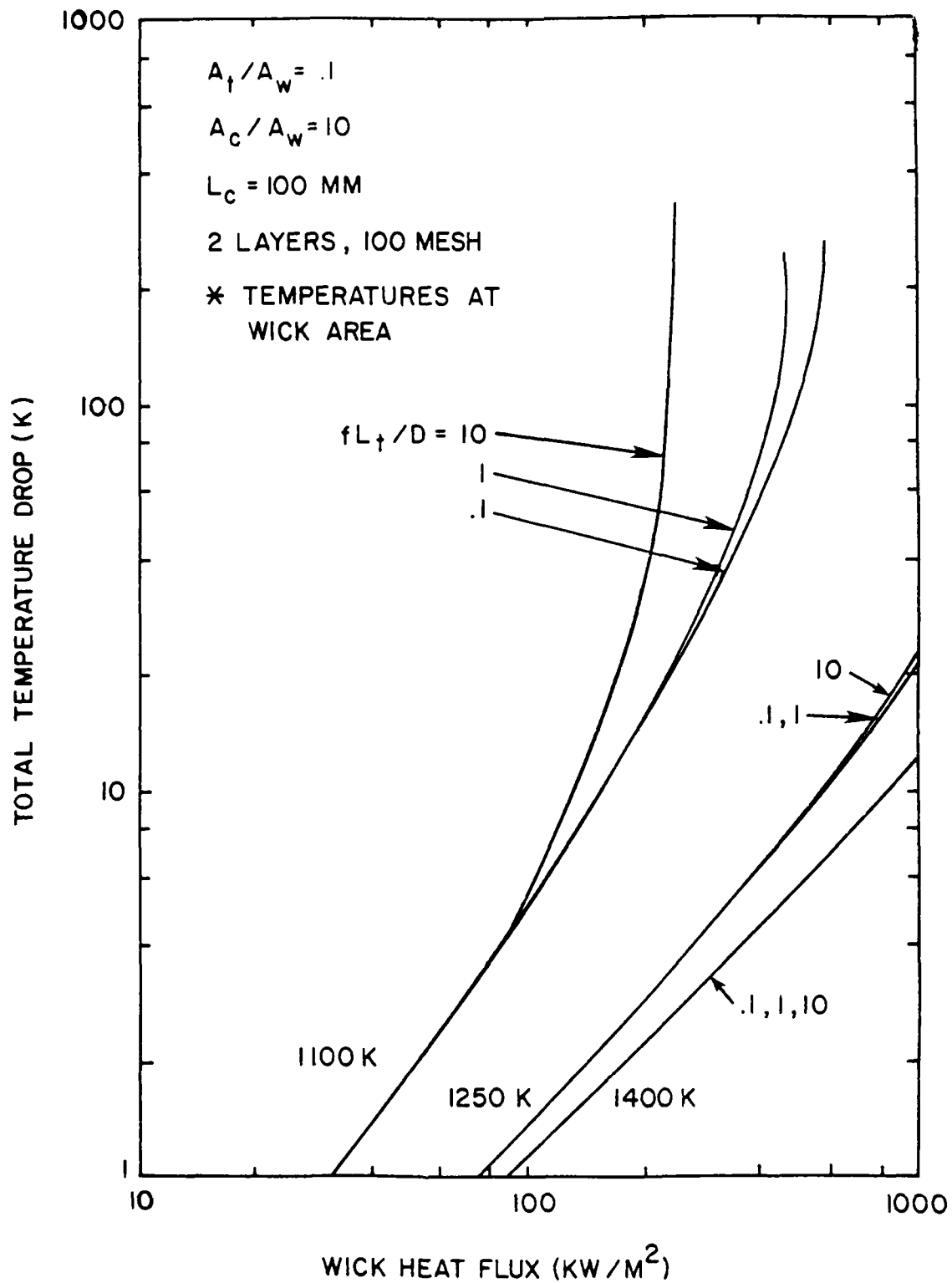


Figure 22 Effect of Flow Losses on System Thermal Performance with No Argon in the Condenser

results obtained for the complete vapor transport system and condenser in the absence of noncondensibles. Figure 23 shows similar results when a noncondensable gas is present. The reference temperature shown on these figures is the temperature at the inlet of the vapor transport tube.

In general, the temperature drop for all steps in the heat transport system increases as the heat flux increases, and as the mean temperature of the vapor decreases. The latter effect is the result of the lower vapor pressure and lower thermal conductivity of liquid lithium at these conditions.

In Figure 22, the results for various values of  $fL_t/D$  are identical at low heat fluxes, however, the temperature drop increases more rapidly for higher values of  $fL_t/D$  at the higher heat fluxes. The results for  $fL_t/D = 10$  at 1100 K illustrate the phenomena of choking in the vapor transport tube. As the heat flux increases, a condition is reached where the temperature drop increases very rapidly with increasing heat flux. Eventually a condition is reached where the heat flux reaches a maximum value, irrespective of the available temperature difference, for the given inlet temperature. At this condition, the vapor transport tube can only deliver the maximum heat flux, irrespective of conditions in the condenser, and the flow at the exit of the transport tube is choked. The maximum heat flux under choked conditions decreases as the friction parameter is increased.

Operation in the choked region may occur during startup of the system when the condenser is at low temperatures. Through choking,

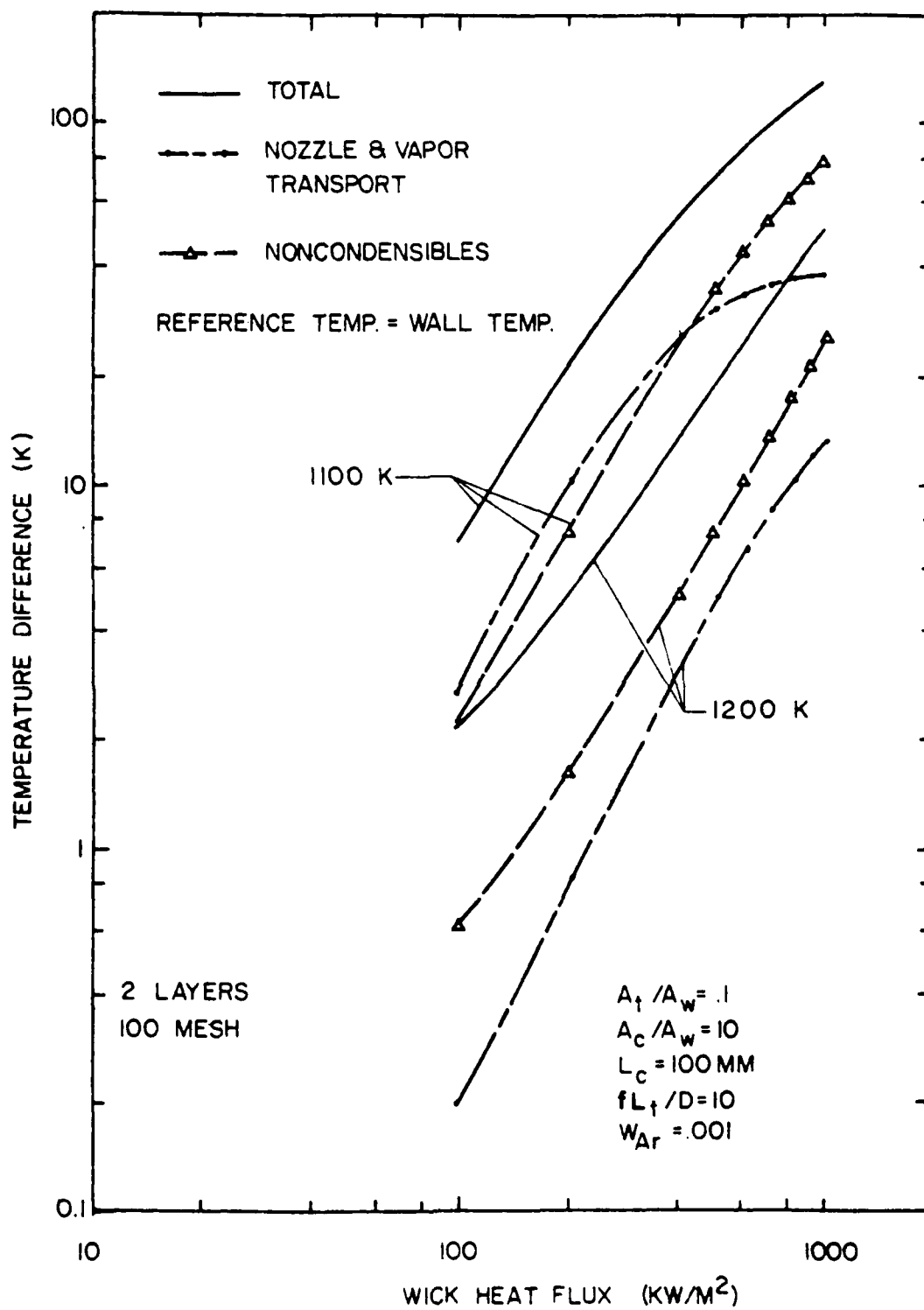


Figure 23 Flow Losses in the Vapor Transport System with Argon in the Condenser

only a limited amount of heat can be supplied to the load, while the remainder of the energy of reaction serves to increase the temperature level of the wick area. As the temperature of the wick increases, the choked heat flux increases as well, as shown in Figure 22. Therefore, more energy is transported to the load as the design wick temperature level is approached, and choking ceases to be a limiting factor. For the arrangements used during the test program discussed earlier,  $fL_t/D$  is small and losses in the vapor transport tube were negligible, except during startup.

In Figure 23, the reference temperature has been transferred to the condenser area, and noncondensibles are considered. There is no choking in the vapor transport system for the temperature levels shown on the figure. The thermal resistance due to the noncondensable gas is sufficiently large so that the total heat flux in the system is not sufficient to cause choking. It is evident that even a low level of noncondensibles can provide a thermal resistance equivalent to that of the film condensation process itself. Higher levels of noncondensibles will be considered in the next section.

### 5.3 Thermal Resistances in Some Typical Systems

Temperature distributions within some typical system are illustrated in Figures 24 and 25. Figure 24 considers operation when there is no noncondensable gas in the system, while Figure 25 considers the effect of noncondensibles. Both figures are constructed for a condenser wall temperature of 1200 K and a heat flux of  $1000 \text{ kW/m}^2$ .

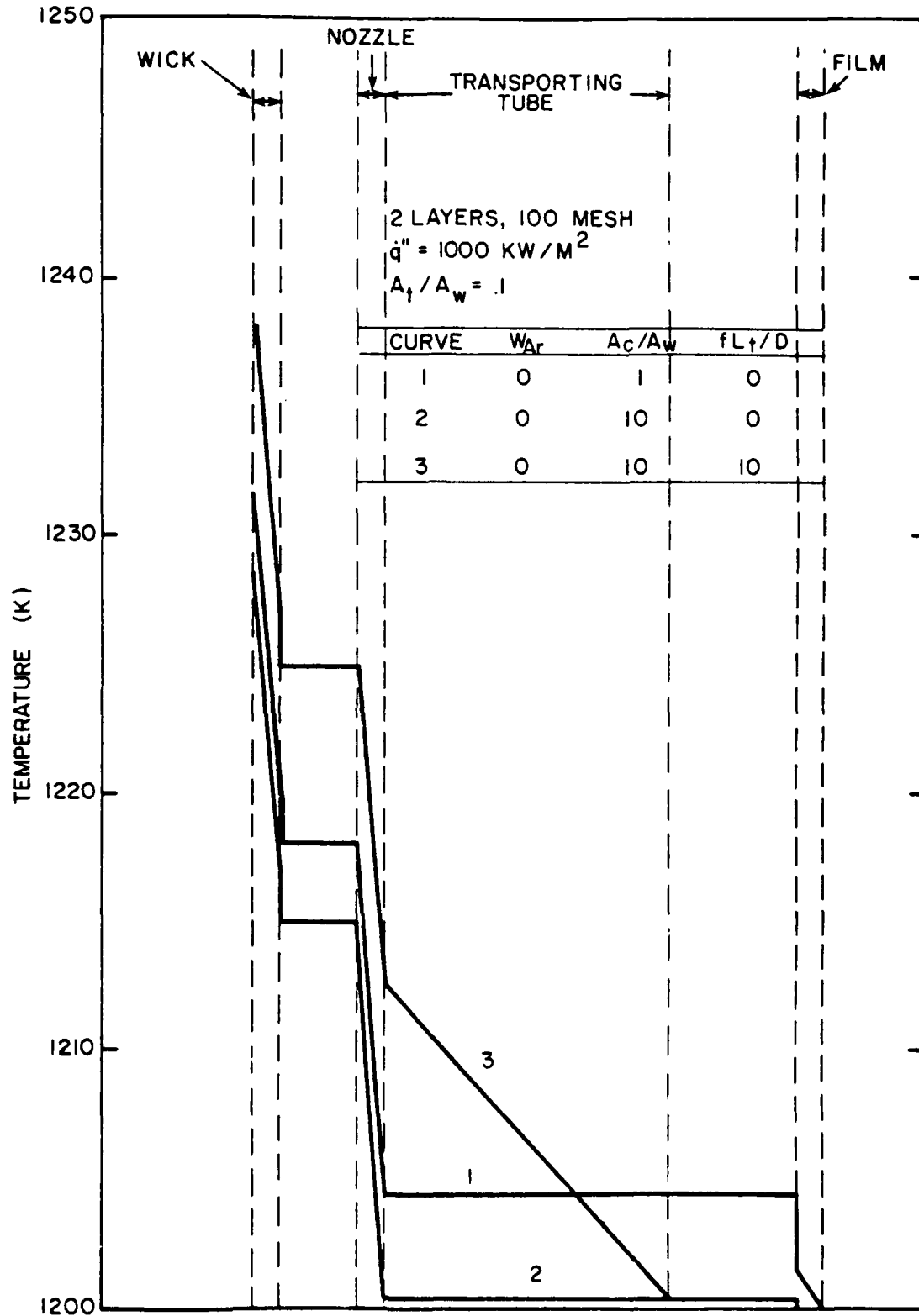


Figure 24 Temperature Distributions in a Reactive-Heat-Pipe with No Argon in the Condenser

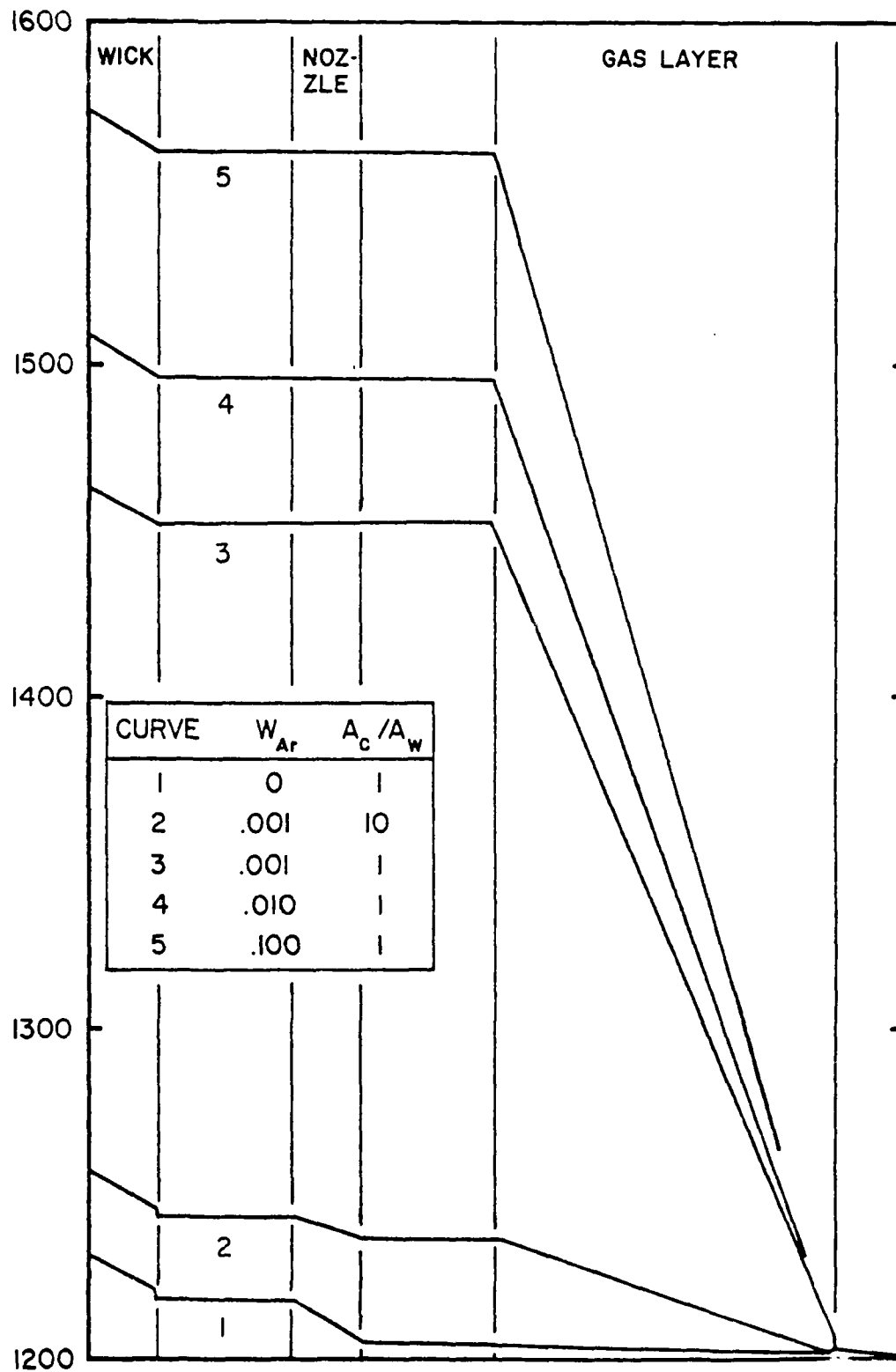


Figure 25 Temperature Distribution in a Reactive-Heat-Pipe with Various Argon Concentrations in the Condenser

The baseline system in Figure 24 is represented by curve 1, which is constructed for a case where the wick area equals the condenser area, the area of the transport tube is .1 that of the wick, and the frictional resistance of the transport tube is negligible. In this case, the total temperature drop is 31.5 C. The major resistances in the system are the temperature drop through the wick and the temperature drop caused by acceleration of the flow into the transport tube.

Curve 2 in Figure 24, involves increasing the condenser area by a factor of 10. This results in only a small reduction in the total temperature drop, since the condenser resistance is not a controlling factor for the baseline system. Curve 3 involves a finite resistance in the vapor transport tube; the effect here is to increase the temperature drop across the transport tube, resulting in an overall temperature drop to the system of 38 K. Therefore, it is evident that the design of various aspects of the system can shift the controlling heat transfer resistance from wick to vapor transport tube to condenser.

Figure 25 compares the same baseline system, with conditions which have various levels of noncondensibles in the condenser. Curve 1 represents the baseline system, with its temperature drop of 31.5 C. When argon is present in the system with a mole fraction of .1 in the condenser area (curve 5), the overall temperature drop in the system increases to 372 C. Reducing the argon mole fraction to .001 (curve 3), only reduces the temperature drop to 262 C. Therefore, the effect of noncondensibles is very nonlinear and a

substantial resistance is provided by very small quantities of noncondensibles. Of all the loss mechanisms examined during this study, it appears that the presence of noncondensable gases in the condenser is one of the most important factors.

There are several ways of overcoming the noncondensable problem. One approach involves reducing the heat flux on the condenser surfaces. For example, the results in Figure 25 for curve 2, indicate that the total temperature drop is reduced to 57 C, for a mole fraction of .001, when the condenser area is increased by a factor of 10. For many types of loads, particularly in the case of gas cycles, limitations on the allowable heat exchanger flux will result in conditions of this type. Another approach involves the use of baffles or constricted vapor flow passages, to increase the vapor velocity past the condenser surface. This increases the surface heat and mass transfer coefficients in the noncondensable layer above the natural convection calculation values used in the present calculations. Baffles also tend to sweep the noncondensable material away from the surface of the condenser. Both of these effects reduce the heat transfer resistance due to noncondensibles. When all these techniques are used, in conjunction with practical levels of control of noncondensibles in the system, acceptable designs should be feasible.

## CHAPTER VI

### SUMMARY AND CONCLUSIONS

#### 6.1 Summary

The overall objective of the present study was to investigate, both analytically and experimentally, the characteristics of a modified liquid metal combustor employing the lithium-sulfur hexafluoride reactant combination. The specific objectives of this study were as follows:

1. Design and test a small scale version of the reactive heat pipe combustor in order to observe its operation.
2. Complete a theoretical analysis of the reactive heat pipe system in order to obtain the design characteristics of the wick, and the heat transport system.

The oxidizer was injected into the space inside the free-standing wick, and reacted with lithium vapor evaporated from the wick. Lithium vapor evaporating from the outer surface of the wick served to transfer thermal energy to the load. The cylindrical combustor wall above the liquid level acted as the condenser surface of the heat pipe. Heat loss from the combustor through the surface was controlled by sweeping them toward a collector, through a baffle system located parallel to the condenser surface.

The system was operated in the wall temperature range 1088-1240 K with wick power densities in the range 0-260 kW/m<sup>2</sup>. No corrosion problems were observed using type 316 stainless steel for the components of the combustor. The capability of the system to operate

under variable load, including idling, as well as restarting, was also demonstrated.

The oxidizer flow rate was varied in order to accommodate different load conditions. At a fixed wall temperature, the temperature and pressure in the reaction space did not vary significantly as the load was changed. The condenser wall temperatures were nearly constant at full-load conditions, which demonstrates the desirable characteristics of the heat pipe configuration. A major practical problem encountered during the testing was the presence of small quantities of noncondensibles in the system. The noncondensibles acted to increase the heat transfer resistance of the condenser. Problems were circumvented by using a noncondensibile collection tube and installing baffles in the system.

The theoretical analysis considers screens of two and four layers with mesh sizes ranging from 30 to 250. System temperatures were varied from 1100-1400 K, and the heat flux through the wick was in the range 0-1000 kW/m<sup>2</sup>. The presence of noncondensibles, as argon, were considered in the mole fraction range 0-.1. The vapor in the condenser, was conservatively considered to condense under free-convection conditions. The pressure drop characteristics in the vapor transport system between the wick and the condenser were also considered.

## 6.2 Conclusions

The major conclusions of the study are as follows:

1. For a given heat flux, the maximum pumping height can be increased by using more layers of screen in order to reduce

the viscous losses. There is an optimum mesh size for given conditions which yields the maximum pumping height; below this size, reduced capillary forces limit performance; above this size, increased viscous forces limit performance.

2. The liquid displacement at the base of the wick increases as the thickness of screen, temperature, and heat flux of the wick is increased. This effect can limit the use of a large number of screens in order to reduce viscous losses.
3. The thermal resistance of the evaporation process, the vapor transport process and the condensation process, increases as the temperature level in the system decreases. At low temperature levels choking can occur in the vapor transport system which limits the energy delivery to the load.
4. The most significant thermal resistance appears to be due to the presence of noncondensibles in the system. The noncondensibles can be controlled by limiting condenser heat fluxes, using a baffle to sweep noncondensibles from the heat exchanger surface [13], and increasing vapor velocities along the surfaces of the condenser in order to reduce the diffusional resistance of the layer of noncondensibles.
5. The experiments demonstrated relatively uniform temperature distributions on a load heat exchanger, easy repair and maintenance of the system, no danger of local subcooling of the wick during high heat loads, compactness of the

combustor, fast start capabilities, and rapid adjustment to load changes. Observations of the combustor after the test did not indicate any substantial degree of corrosion, however, the present test periods were relatively short, extending only to four hours of operation. Longer duration testing is desirable, in order to fully evaluate the effects of corrosion.

### 6.3 Recommendations for Further Study

In many practical applications higher wick pumping heights than can be accommodated by the design considered in this study would be desirable. The analysis indicates that the use of arterial wicks would provide such capability, and the feasibility of systems of this type should be examined.

With regard to the analysis, the present investigation has been limited to natural convection conditions in the condenser. This is the most conservative estimation of the effect of noncondensibles and forced convection phenomena should be considered as well. The analysis has also been limited to the case where the quantity of noncondensibles in the system is sufficiently large so that the increased concentration at the surface of the condenser does not significantly deplete the ambient concentration of noncondensibles. Further analysis would be desirable at the limit of low levels of noncondensibles, following the lines indicated by the work of Rohsenow and Kroger [29].

## BIBLIOGRAPHY

1. Pauliukonis, R. S., "Fuel System Comprising Sulfur Hexafluoride and Lithium Containing Fuel," United States Patent 3, 325, 318, June 13, 1967.
2. Van der Sluijs, W. L. N., "A Lithium/Sodium/Sulphur Hexafluoride Heat Source in Combination with a Stirling Engine as a Propulsion System for Small Submersibles," Proceedings of Tenth Intersociety Energy Conversion Engineering Conference, pp. 1031-1037, 1975.
3. Groff, E. G., "Characteristics of a Steadily Operating Metal Combustor," Ph.D. Thesis, The Pennsylvania State University, University Park, Pennsylvania, 1976.
4. Uhlemann, H., Spigt, C. L., and Hermans, M. L., "The Combination of Stirling Engine with a Remotely Placed Heat Source," Proceedings of Ninth Intersociety Energy Conversion Engineering Conference, pp. 620-629, 1974.
5. Biermann, U. K. P., "The Lithium/Sulfurhexafluoride Heat Source in Combination with a Stirling Engine as an Environmental Independent Underwater Propulsion System," Proceedings of Tenth Intersociety Energy Conversion Engineering Conference, pp. 1023-1030, 1975.
6. Blakeslee, T., Groff, E. G., Faeth, G. M., and Olson, D.R., "A Study of a Liquid Metal Thermal Energy Source," Quarterly reports: March 1 to May 30, June 1 to August 31, September 1 to November 30, 1976," Contract No. N00600-74-C-0033, Advanced Research Projects Agency, ARPA Order No. 2150, Program Code No. 2N10, Mechanical Engineering Department, The Pennsylvania State University, 1976.
7. Blakeslee, T., Groff, E., Faeth, G. M., and Olson, D. R., "A Study of a Liquid Metal Thermal Energy Source, Annual Report: September 1, 1973 to August 31, 1974," Contract No. N00600-74-C-0033, Advanced Research Projects Agency, ARPA Order No. 2150, Program Code No. 2N10, Mechanical Engineering Department, The Pennsylvania State University, September, 1974.
8. Faeth, G. M., Kuo, K. K., and Olson, D. R., "A Study of a Liquid Metal Thermal Energy Source, Final Report: August 23, 1972, to August 23, 1973," Contract No. N00600-73-C-0113, Advanced Research Projects Agency, ARPA Order No. 2150, Program Code No. 2N10, Mechanical Engineering Department, The Pennsylvania State University, 1973.
9. Avery, J. A. and Faeth, G. M., "Combustion of a Submerged Gaseous Oxidizer Jet in a Liquid Metal," Fifteenth Symposium (International) on Combustion, The Combustion Institute, Pittsburgh, pp. 501-512, 1974.

10. Blakeslee, T., "Laminar Free-Convective Combustion of a Liquid Metal from a Wick," Ph.D. Thesis, The Pennsylvania State University, University Park, Pennsylvania, 1977.
11. Vargaftu, N. B., Tables on the Thermophysical Properties of Liquid and Gases, Hemisphere, New York, 1975.
12. Dunn, P. D. and Reay, D. A., Heat Pipes, Pergamon Press, Oxford, 1st ed., 1976.
13. Collier, John T., Convective Boiling and Condensation, McGraw-Hill, New York, 1972.
14. Tien, C. L. and Sun, K. H., "Minimum Meniscus Radius of Heat Pipe Wicking Materials," Int. J. of Heat Mass Transfer, Vol. 14, 1971, pp. 1853-1855.
15. Feldman, K. T., Jr., "The Heat Pipe: Theory, Design, and Application," Heat Pipe Technology, A five-day short course and workshop presented by the College of Engineering and the Technology Application Center at The University of New Mexico, Albuquerque, January 6-10, 1971, Part I.
16. Feldman, K. T., Jr. and Heat Pipe Department, Energy Conversion System Inc., Albuquerque, New Mexico, Heat Pipe Analysis, Design and Experiments, Scott-Engineering Sciences, Automatic Sprinkler Corporation, Dompano Beach, Florida, Publication No. 9068, December, 1968.
17. Ferrell, J. K., Winston, H. H. and Davis R., "Heat Pipe Wick Properties and Performance," Department of Chemical Engineering, North Carolina State University, Raleigh, October 1973, pp. 4-7.
18. Davison, H. W., "Compilation of Thermophysical Properties of Liquid Lithium," NASA TN D-4650, Lewis Research Center, Cleveland, Ohio, July, 1968.
19. Schrage, R. W., A Theoretical Study of Interphase Mass Transfer, Columbia University Press, New York, 1953.
20. Meyrial, P. M., Morin, M. M., Wilcox, S. J., and Rohsenow, W. M., "Effect of Precision of Measurement on Reported Condensation Coefficients for Liquid Metals - Including Condensation Data on a Horizontal Surface," Proceedings in the 4th Int. Heat Transfer Conference, Paris-Versailles, 1970. Heat Transfer 1970, Elsevier, Amsterdam, 1970, Vol. VI, Cs 1.1.
21. Shapiro, A. H., The Dynamics and Thermodynamics of Compressible Fluid Flow, Vol. I, Ronald Press, New York, 1955, Chapter 6.

22. Akers, W. W., Davis, S. H., Crawford, J. E., "Condensation of a Vapor in the Presence of a Noncondensable Gas," Chemical Engineering Progress Symposium Series 56 (30), pp. 139-144.
23. Sparrow, E. M. and Eckert, E. R. G., "Effects of Superheated and Noncondensable Gases on Laminar Film Condensation," A.I.Ch.E. Journal, Vol. 7, No. 3, pp. 473-477, 1961.
24. Sparrow, E. M. and Lin, S. H., "Condensation Heat Transfer in the Presence of a Noncondensable Gas," J. of Heat Transfer, Vol. 86, No. 2, pp. 430-436, 1964.
25. Bird, R. B., Stewart, W. E. and Lightfoot, E. N., Transport Phenomena, John Wiley and Sons, Inc., 1960.
26. Sherwood, T. K., Pigford, R. L. and Wilke, C. R., Mass Transfer, McGraw-Hill, New York, 1975.
27. McAdams, W. H., Heat Transmission, McGraw-Hill, New York, 1954.
28. Chapman, A. J., Heat Transfer, Macmillan, New York, 2nd ed., 1967.
29. Rohsenow, W. M. and Kroger, D. G., "Film Condensation of Saturated Potassium Vapor," Int. J. Heat Mass Transfer, Vol. 10, pp. 1891-1894, 1967.

## APPENDIX A

### CALCULATION OF THE THERMAL RESISTANCE OF CONDENSATION FOR TEST 3

To calculate the thermal resistance of condensation, the combustor was run at a steady state condition so that the heat generated was equal to the heat output. To simplify the calculations, the upper edge of the radiation shield is taken to be above the level of the liquid surface, and the top surface of the combustor is insulated. Because the heat conduction through the insulation is small, we can assume that all the heat is transferred through the exposed combustor wall. The thermal resistance at condenser can be defined as follows:

$$\begin{aligned} r_c &\equiv \frac{1}{h_c A_{ex}} \\ &= \frac{T_g - T_{ci}}{Q} \end{aligned} \quad (A.1)$$

As discussed in Section 3.2, we can neglect the effect of heat conduction from the condenser wall below the upper edge of the shield due to the rather uniform temperature distribution. The height of the condenser wall above the liquid surface can be directly measured by vision or, more precisely, calculated from the properties of the reactants and the products as described in Reference 3.

The temperature of the inner surface of the condenser is

$$T_{ci} = T_{co} + \frac{Q \ln \left( \frac{D_{co}}{D_{ci}} \right)}{2\pi L_{ex} k_c} \quad (A.2)$$

where

$$\dot{Q} = \dot{m}_{ox} Q_r$$

From Figure 5, we can get the temperature of the inner surface of the wick by measuring the combustor pressure. Equation (4.20) and (4.23) yield the temperature of the outer surface of the wick. If the radial vapor velocity is small, we can simply take the temperature of the outer surface of the wick to be the stagnant temperature outside the condenser.

At 80 minutes from start-up in Test 3, the temperature distribution of the outer surface of the condenser ranged from 1150 K to 1158 K, the combustor pressure inside the wick cylinder was 18 mm Hg, the oxidizer flow rate was 1.32 Kg/hr and the exposed length of the condenser was 115 mm, which was approximately equal to the height above the liquid surface. The comparison of the actual and the expected thermal resistances at this instant of time is computed in the following.

From Figure 5, we know the inner surface temperature of the wick is approximately 1220 K. The thermal conductivity of the condenser wall is 24 W/m-k [28]. The wick heat flux is approximately 260 Kw/m<sup>2</sup>. From Equation (A.2), the inner surface temperature of the condenser is 1189 K. Following the analysis in Section 4.1, the temperature drop which includes the drop through the wick and the jump due to nonequilibrium evaporation is 3.92 K. The bulk vapor velocity leaving the wick surface is

$$\begin{aligned} V &= \frac{\dot{q}''}{h_{fg} \rho_{L1}} \\ &= \frac{260}{20818 \times 1.494 \times 10^{-3}} \quad \text{m/s} \\ &= 8.36 \quad \text{m/s} \end{aligned}$$

Since  $V$  is small, we can take  $(1220 - 3.92)\text{K}$  to be the temperature right before the condensation process. Then the total temperature drop through the condensation process is 27 K. If there was no noncondensable gas in the combustor, following the analysis in Section 4.1, the temperature drop for the condensation process is 1.16 K. The resistance ratio of the experimental and the expected value is approximately 24.

## APPENDIX B

### CALCULATION OF PROPERTIES FOR GAS MIXTURES

#### B.1 Grashof Number

The Grashof number is defined as

$$Gr = \frac{L_c^3 (\Delta\rho/\rho) g \rho^2}{\mu^2} \quad (B.1)$$

In order to calculate the density terms, the vapor gas mixtures is assumed to be an imperfect gas. The total pressure across the boundary layer is a constant, therefore,

$$\frac{\Delta\rho}{\rho} = 1 - \frac{\bar{M}_g}{\bar{M}_{g'}} \frac{T_{g'}}{T_g} \frac{Z_{g'}}{Z_g} \quad (B.2)$$

where  $Z$  is the compressibility factor. For condensation processes, which occur at moderately low pressures, we can take  $Z_{g'}/Z_g \sim 1$  [24], yielding

$$\frac{\Delta\rho}{\rho} = 1 - \frac{\bar{M}_g}{\bar{M}_{g'}} \frac{T_{g'}}{T_g} \quad (B.3)$$

The molecular weight of the mixtures can be calculated as follows

$$\bar{M}_g = (1 - W_{Ar,g}) \bar{M}_{Li} + W_{Ar,g} \bar{M}_{Ar} \quad (B.4)$$

$$\bar{M}_{g'} = (1 - W_{Ar,g'}) \bar{M}_{Li} + W_{Ar,g'} \bar{M}_{Ar} \quad (B.5)$$

Where  $W_{Ar,g}$  and  $W_{Ar,g'}$  are the mole fractions of noncondensable gas in the space far from the liquid film surface and at the surface, respectively. The mole fractions can be calculated from the

following equations

$$W_{Ar,g} = 1 - \frac{P_{Li,g}}{p} \quad (B.6)$$

$$W_{Ar,g'} = 1 - \frac{P_{Li,g'}}{p} \quad (B.7)$$

The viscosity of argon-lithium vapor mixtures at low density can be well approximated by Wilkes' semi-empirical formula [25].

$$\mu_{mix} = \frac{W_{Li}\mu_{Li}}{W_{Li} + W_{Ar}\phi_{Li-Ar}} + \frac{W_{Ar}\mu_{Ar}}{W_{Li}\phi_{Ar-Li} + W_{Ar}} \quad (B.8)$$

in which

$$\phi_{Li-Ar} = \frac{1}{\sqrt{8}} \left( 1 + \frac{\bar{M}_{Li}}{\bar{M}_{Ar}} \right)^{-0.5} \left[ 1 + \left( \frac{\mu_{Li}}{\mu_{Ar}} \right)^{0.5} \left( \frac{\bar{M}_{Ar}}{\bar{M}_{Li}} \right)^{0.25} \right]^2 \quad (B.9)$$

$$\phi_{Ar-Li} = \frac{1}{\sqrt{8}} \left( 1 + \frac{\bar{M}_{Ar}}{\bar{M}_{Li}} \right)^{-0.5} \left[ 1 + \left( \frac{\mu_{Ar}}{\mu_{Li}} \right)^{0.5} \left( \frac{\bar{M}_{Li}}{\bar{M}_{Ar}} \right)^{0.25} \right]^2 \quad (B.10)$$

and  $\mu_{Ar}$  and  $\mu_{Li}$  are the viscosity of argon and lithium vapor at the system temperature and pressure.

The densities of the argon-lithium vapor mixture are determined by

$$\rho_{mix} = p \bar{M}_{mix} / RT \quad (B.11)$$

or

$$\rho_{mix} = p(W_{Li} \bar{M}_{Li} + W_{Ar} \bar{M}_{Ar}) / RT \quad (B.12)$$

Considering the changes of molecular weight of the lithium vapor due to the presence of diatomic molecules, the correlation for the molecular weight of saturated lithium vapor is applied.

### B.2 Prandtl Number

The Prandtl number is defined as

$$\text{Pr} = \frac{\mu C_p}{k} \quad (\text{B.13})$$

The value of  $\mu_{\text{mix}}$  has already been given in Equation (B.8). The value of  $k_{\text{mix}}$  is given by a semi-empirical formula similar to Equation (B.8) [25].

$$k_{\text{mix}} = \frac{W_{\text{Li}} k_{\text{Li}}}{W_{\text{Li}} + W_{\text{Ar}} \phi_{\text{Li-Ar}}} + \frac{W_{\text{Ar}} k_{\text{Ar}}}{W_{\text{Li}} \phi_{\text{Ar-Li}} + W_{\text{Ar}}} \quad (\text{B.14})$$

where  $\phi_{\text{Li-Ar}}$  and  $\phi_{\text{Ar-Li}}$  were given by Equations (B.9) and (B.10).

The specific heat of argon-lithium vapor mixtures can be calculated from

$$C_{p_{\text{mix}}} = (W_{\text{Li}} \bar{C}_{p_{\text{Li}}} + W_{\text{Ar}} \bar{C}_{p_{\text{Ar}}}) / (W_{\text{Li}} \bar{M}_{\text{Li}} + W_{\text{Ar}} \bar{M}_{\text{Ar}}) \quad (\text{B.15})$$

where  $\bar{C}_{p_{\text{Li}}}$  and  $\bar{C}_{p_{\text{Ar}}}$  are taken as the average properties in the range 1000-1400 K.

### B.3 Schmidt Number

The theoretical equation for the mutual diffusion coefficient in a low pressure argon-lithium vapor mixture is [26]

$$D_{\text{Li-Ar}} = \frac{1.858 \times 10^{-7} T^{1.5} (1/\bar{M}_{\text{Li}} + 1/\bar{M}_{\text{Ar}})^{0.5}}{p \bar{\sigma}_{\text{Li-Ar}}^2 \Omega_D} \quad (\text{B.16})$$

where  $D_{\text{Li-Ar}}$  is in  $\text{m}^2/\text{s}$ ,  $p$  in atm.,  $\bar{\sigma}_{\text{Li-Ar}}$  in Å.  $\Omega_D$  is the collision integral and is a function of  $\bar{k}T/\epsilon_{\text{Li-Ar}}$ . The values of this parameter can be found in Table 2.2 of Reference [26]. The constants  $\epsilon_{\text{Li-Ar}}$  and  $\bar{\sigma}_{\text{Li-Ar}}$  are obtained by use of the following combining rules

$$\frac{\epsilon_{\text{Li-Ar}}}{\bar{k}} = \left( \frac{\epsilon_{\text{Li}}}{\bar{k}} \frac{\epsilon_{\text{Ar}}}{\bar{k}} \right)^{1/2} \quad (\text{B.17})$$

$$\bar{\sigma}_{\text{Li-Ar}} = \frac{1}{2} (\bar{\sigma}_{\text{Li}} + \bar{\sigma}_{\text{Ar}}) \quad (\text{B.18})$$

The Lennard-Jones potential parameters  $\bar{\sigma}_{\text{Ar}}$  and  $\epsilon_{\text{Ar}}/\bar{k}$  can be found in Table 2.3 of Reference [26]. They are

$$\bar{\sigma}_{\text{Ar}} = 3.542 \text{ \AA}$$

$$\frac{\epsilon_{\text{Ar}}}{\bar{k}} = 93.3 \text{ K}$$

The above parameters are not available for lithium vapor, therefore, we use the following approximate rules [26]

$$\frac{\epsilon_{\text{Li}}}{\bar{k}} = 0.75 (T_c)_{\text{Li}} \quad (\text{B.19})$$

$$\bar{\sigma}_{\text{Li}} = \frac{5}{6} (V_c)_{\text{Li}}^{1/3} \quad (\text{B.20})$$

where  $T_c$  is in K,  $V_c$  is in  $\text{cm}^3/\text{g mole}$  and  $\bar{\sigma}_{\text{Li}}$  is in  $\text{\AA}$ . From Table 3 we obtain

$$\frac{\epsilon_{\text{Li}}}{\bar{k}} = 2850 \text{ K}$$

$$\bar{\sigma}_{\text{Li}} = 3.424 \text{ \AA}$$

yielding

$$\bar{\sigma}_{\text{Li-Ar}} = 3.483 \text{ \AA}$$

$$\frac{\epsilon_{\text{Ar-Li}}}{\bar{k}} = 515.66 \text{ K}$$

Since  $\Omega_D$  changes very slightly for an argon and lithium mixture in the range of the present calculations, we employ the average value  $\Omega_D = 1.028$  for the calculations.

For the diffusion of lithium vapor in an argon layer, the Schmidt Number is given by

$$Sc_{Li-Ar} = \frac{\mu_{Ar}}{\rho_{Ar} D_{Li-Ar}} \quad (B.21)$$

Distribution and Addressee Listing

<u>Addressee</u>	<u>Copies</u>
Director Advanced Research Projects Agency Architect Building 1400 Wilson Blvd. Arlington, VA 22209	3/0
Officer in Charge David W. Taylor Naval Ship Research and Development Center Annapolis Laboratory Annapolis, Maryland 21402 Attn: Mr. S. Cox, Code 2724	9/1
CDR C. E. Moore, OPNAV 233 Chief of Naval Operations, Off of the Room 5E577 Pentagon Washington, D. C. 20301	1/0
TACTEC Battelle Columbus Laboratories 505 King Avenue Columbus, Ohio 43201	1/0
Dr. Eugene C. Gritton The Rand Corporation 1700 Main Street Santa Monica, CA 90406	5/0